Friedrich-Alexander-Universität
Naturwissenschaftliche Fakultät

Master's Thesis
in Physics

Ground-state properties of one-dimensional Dicke-Ising models

Jonas Leibig

Supervisor: *Kai Phillip Schmidt*
Chair for Theoretical Physics V

Submission date: *15.09.2025*

Abstract

We investigate the ground-state properties of the Dicke-Ising model on the simple chain and the frustrated sawtooth chain using an effective self-consistent matter Hamiltonian. Our approach combines Density Matrix Renormalization Group (DMRG) simulations with Numerical Linked-Cluster Expansions (NLCE) and perturbative series expansions.

For the ferromagnetic chain, we determine the multicritical point, located at $\varepsilon/\omega_c \approx 0.200124$, where the superradiant transition changes from second to first order with high precision, in excellent agreement with quantum Monte Carlo benchmarks. For antiferromagnetic Ising interactions, we identify the antiferromagnetic superradiant phase, establish its phase boundaries, and resolve the transition orders: a continuous transition into this phase and a first-order transition out of it.

On the sawtooth chain, we derive a dual formulation of the transverse-field Ising model and verify it via exact diagonalization. Extending to the Dicke-Ising model, we show that without a longitudinal field the system enters the superradiant phase at infinitesimal light-matter coupling (disorder-by-disorder), while finite longitudinal fields lift the frustration-induced degeneracy and lead to magnetically ordered phases followed by sharp first-order superradiant transitions.

These results highlight how frustration, spin-photon coupling, and external fields conspire to generate unconventional quantum phases, and demonstrate the power of NLCE+DMRG for coupled light-matter systems.

Kurzzusammenfassung

Wir untersuchen die Grundzustandseigenschaften des Dicke–Ising-Modells auf der einfachen Kette und der frustrierten Sägezahnkette mithilfe eines effektiven selbstkonsistenten Materie-Hamiltonians. Unsere Methode kombiniert Dichtematrix-Renormierungsgruppen (DMRG) Simulationen mit der numerischen Linked-Cluster Entwicklung (NLCE) sowie perturbativen Reihenentwicklungen.

Für die ferromagnetische Kette bestimmen wir den multikritischen Punkt, an dem der superradianten Phasenübergang von zweiter in erster Ordnung übergeht, mit hoher Präzision bei $\varepsilon/\omega_c \approx 0.200124$ in ausgezeichneter Übereinstimmung mit Quanten-Monte-Carlo-Ergebnissen. Im antiferromagnetischen Fall identifizieren wir die antiferromagnetische superradianten Phase, bestimmen ihre Phasengrenzen und charakterisieren die Übergänge: einen kontinuierlichen Eintritt in diese Phase und einen ersten Ordnungsübergang beim Verlassen der Phase.

Für die Sägezahnkette leiten wir eine duale Formulierung des Transversal-Ising-Modells her und überprüfen deren Gültigkeit mittels exakter Diagonalisierung. In der Erweiterung zum Dicke-Ising-Modell zeigen wir, dass das System ohne Longitudinalfeld bereits bei infinitesimaler Kopplung in die superradianten Phase übergeht (Disorder-by-Disorder), während ein endliches Longitudinalfeld die frustrierte Entartung aufhebt und zu magnetisch geordneten Phasen sowie zu abrupten Übergängen in die superradianten Phase führt.

Diese Ergebnisse verdeutlichen, wie Frustration, Spin-Photon-Kopplung und äußere Felder unkonventionelle Quantenphasen hervorbringen, und zeigen die Leistungsfähigkeit von NLCE+DMRG für Systeme mit Licht-Materie Wechselwirkung.

Contents

1. Introduction **1**

2. Theoretical background **5**

2.1. Light-Matter coupling . . . 5
2.2. Regimes of light-matter coupling . . . 5
2.3. Experimental Realizations . . . 6
2.4. The Dicke Model . . . 6
2.5. The Ising model . . . 9
2.6. Dicke-Ising Model . . . 10
2.6.1. Phase diagram of the Dicke-Ising model . . . 11
2.6.2. Influence of the diamagnetic A^2-term on the Dicke–Ising model . . . 12
2.7. Self-Consistent Effective matter Hamiltonian . . . 13
2.7.1. Displacement transformation . . . 13
2.7.2. Mean-field decoupling . . . 16

3. Methods **17**

3.1. Non-Perturbative Linked-Cluster Expansion . . . 17
3.2. Exact Diagonalization . . . 19
3.3. Density Matrix Renormalization Group . . . 19
3.4. High-order series expansion . . . 20

4. Multicritical Point in the Ferromagnetic Dicke-Ising chain **22**

4.1. Self-consistent solution for ferromagnetic Ising couplings . . . 22
4.2. Determining the order of the quantum phase transition . . . 23
4.3. Examples: first- vs. second-order transitions . . . 24
4.4. Locating the multicritical point . . . 25

5. Antiferromagnetic Superradiance in the Dicke-Ising chain **27**

5.1. Solving the self-consistency for antiferromagnetic Ising couplings . . . 27
5.2. Results . . . 28

6. Frustration Phenomena on the Sawtooth Chain **31**

6.1. TFIM on the Sawtooth Chain . . . 31
6.1.1. Frustrated Ising Limit . . . 31

6.2. Dicke-Ising model on the sawtooth chain 36
6.2.1. Results 36
6.2.2. Series expansion in the strong coupling limit 38

7. Conclusion **43**

8. Outlook **44**

A. DMRG Parameters **46**

B. Exact the solution of the quantized transverse field Ising model for the chain geometry **47**

Bibliography **48**

1. Introduction

The interaction between light and matter has been a central theme in both quantum optics and condensed matter physics since the early days of quantum theory. One of the first quantum-mechanical descriptions of this interaction was formulated by Rabi in 1936, who considered a two-level atom in an oscillating field and predicted coherent oscillations of the atomic population under resonance, a phenomenon now known as Rabi oscillations (see, e.g., historical overviews [1, 2]). Building on these ideas, Dicke in 1954 introduced a model of N two-level atoms interacting collectively with a single radiation mode [3]. Dicke's work revealed that an ensemble of atoms can behave as a single coherent emitter, leading to the phenomenon of *superradiance* – an enhanced, collective burst of radiation emitted when atoms act in union. The Dicke model, consisting of a collection of spins (two-level atoms) coupled uniformly to a mode of the electromagnetic field, soon became a paradigmatic model for collective light–matter interactions. In the thermodynamic limit of many atoms, it was found to exhibit a *phase transition* to a superradiant phase, wherein the ground state develops a macroscopic photon population and collective dipole order [4, 5]. This superradiant phase transition is an archetype of equilibrium quantum phase transitions in light–matter systems. We note that a "no-go" theorem once argued that the electromagnetic A^2 term prevents a true ground-state superradiance [6]. However, circuit QED implementations and modern analyses have clarified conditions under which superradiant-like criticality can emerge [7, 8].

Over subsequent decades, the Dicke model and its variations have been realized and explored across a wide range of physical platforms. In the realm of *cavity quantum electrodynamics (QED)*, experiments with single atoms in high-finesse optical cavities reached the strong-coupling regime where an atom can exchange a photon with the cavity many times before decoherence. By the 2000s, many-atom cavity systems were engineered to specifically test Dicke-model physics (see [1] for a review). In parallel, solid-state implementations of light–matter systems flourished. In particular, *circuit QED* – the microwave analogue of cavity QED with superconducting qubits as artificial atoms – demonstrated strong and even ultrastrong coupling between microwave photons and qubits on a chip [9]. These advances underscore the broad relevance of Dicke's collective coupling paradigm in modern quantum technology.

Light–matter interaction models have also become integral in condensed matter contexts. A prominent example is the physics of exciton–polaritons in semiconductor microcavities: when excitons (bound electron–hole pairs in a semiconductor) strongly couple to cavity

photons, the resulting hybrid quasiparticles (polaritons) inherit characteristics of both light and matter. The first observation of the characteristic mode splitting (Rabi splitting) in a semiconductor microcavity by Weisbuch *et al.* [10] confirmed that the strong-coupling regime can be achieved in solid-state systems. In subsequent years, exciton–polaritons were found to undergo Bose–Einstein condensation at low temperature, forming a macroscopically occupied coherent state [11]. Such phenomena illustrate how the concepts of collective light–matter coupling extend into the domain of quantum materials. An emerging frontier is the engineering of *cavity quantum materials*, where the vacuum electromagnetic field of a cavity is used to modify the properties of a many-body system – from chemistry under vibrational strong coupling [12] to proposals and demonstrations of cavity-modified phases in quantum materials [13].

Given this background, it is natural to ask what happens when one goes beyond the idealized limits of the Dicke model. In the standard Dicke model, the atoms (spins) do not interact with each other except through the collective coupling to the photon mode. However, in many physical systems the constituents do possess direct interactions – for example, dipole–dipole interactions between atoms, exchange interactions between spins in a solid, or Josephson couplings between superconducting qubits. To capture such scenarios, we consider the *Dicke–Ising model* [14, 15], an extension of the Dicke model that incorporates a spin–spin interaction of the Ising type. In this model, each two-level system (spin-$\frac{1}{2}$) is coupled to a common photon mode and to its neighboring spins along a one-dimensional lattice via an Ising coupling term. The Dicke–Ising Hamiltonian thus combines two key ingredients: the collective light–matter interaction responsible for superradiance, and the local spin–spin interactions responsible for magnetic ordering (ferromagnetism or antiferromagnetism). This richer model is expected to exhibit a variety of possible ground states and phase transitions, arising from the competition or coexistence of photon-mediated collective order and intrinsic spin order. For example, a sufficiently strong Ising coupling may favor a ferromagnetically ordered spin state with no photons (a spin-ordered, "normal" phase), whereas a sufficiently strong light–matter coupling may favor a superradiant phase where the spins collectively polarize along the field and the cavity contains a macroscopic photon number. In between, mixed phases can occur – e.g. a superradiant antiferromagnet where both the spins are ordered and the field is populated – and the phase boundaries between these regimes can be nontrivial. Indeed, theoretical work has begun to map out the spectra and phase structure of such coupled spin–photon models, finding evidence of multiple excitation branches (polaritons) and phase transitions without analog in the pure Dicke or pure Ising limits [15, 16]. The inclusion

of spin–spin interactions can also change the nature of the superradiant transition itself, potentially altering its order (continuous vs. first-order) or critical exponents, and can lead to new critical points where different orders meet. Beyond these earlier studies, more recent work has provided complementary insights: Schellenberger and Schmidt have shown that broad classes of correlated spin–photon systems can be mapped onto exactly solvable Dicke-type models, including the Dicke–Ising case [17]. Langheld *et al.* employed a wormhole algorithm quantum Monte Carlo simulation to obtain essentially exact quantum phase diagrams of Dicke–Ising models [18], while Koziol *et al.* demonstrated how the intricate devil's staircase structures characterizing long-range versions of the model melt under quantum fluctuations [19].

An especially intriguing aspect emerges when the spin interactions are *frustrated*. Frustration refers to the inability of a spin system to satisfy all pairwise interactions simultaneously, often due to geometric constraints, and it is known to give rise to highly degenerate ground states in the classical limit and strong quantum fluctuations [20]. In this thesis, we specifically consider the *sawtooth chain*, a simple one-dimensional frustrated geometry built from corner-sharing triangles. For the transverse-field Ising model on this lattice it is well established that quantum fluctuations do not stabilize order but instead preserve disorder — a phenomenon known as *disorder by disorder* [21]. It is therefore particularly interesting to investigate whether this mechanism persists in the Dicke–Ising model, where spins are additionally coupled to a common photon mode. In contrast, on an *unfrustrated linear chain* with antiferromagnetic interactions, the spins form a magnetic ordered ground state, so a finite threshold of light–matter coupling is required to destabilize that order in favor of a superradiant phase. Thus, frustration is expected to qualitatively alter the phase diagram and may also lead to additional phase transitions or multicritical behavior.

In this thesis, we investigate these questions by systematically studying the ground-state properties of the Dicke–Ising model on two one-dimensional lattices: the standard *simple chain* (unfrustrated) and the *sawtooth chain* (frustrated). Throughout, the Dicke–Ising model is treated within an effective self-consistent matter Hamiltonian obtained by integrating out the photon degrees of freedom. On the simple chain, we employ a combination of Density Matrix Renormalization Group (DMRG) and Numerical Linked-Cluster Expansions (NLCE) to explore both ferromagnetic and antiferromagnetic regimes: in the ferromagnetic case we search for the *multicritical point* at which the order of the superradiant quantum phase transition changes, while in the antiferromagnetic case we examine the emergence of an *antiferromagnetic superradiant phase*, previously identified in one dimension by Langheld *et*

al. [18]. For the sawtooth chain, we first derive a dual formulation of the transverse-field Ising model, and then extend the analysis to the Dicke–Ising model using DMRG with NLCE and high-order series expansions.

2. Theoretical background

This section closely follows the general structure and key concepts presented in the review by Frisk Kockum *et al.* [2], which provides an accessible introduction to different light-matter coupling regimes and their experimental realizations.

2.1. Light-Matter coupling

The interaction between light and matter is one of the central themes in quantum optics, condensed-matter physics, and quantum technologies. It involves the coupling of electromagnetic fields (e.g. cavity modes) to material excitations such as atoms or spins. Most of the dynamics of the electromagnetic field can be described perturbatively by first-order (absorption, emission) or second-order (scattering) processes due to the small value of the fine-structure constant α [2].

Although the fine-structure constant α is fixed by nature, Purcell showed in 1946 that the strength of light–matter interaction can be modified by tailoring the emitter's electromagnetic environment [22]. This insight laid the foundation for the field now known as cavity quantum electrodynamics (cQED).

2.2. Regimes of light-matter coupling

Depending on the strength of the light-matter coupling g relative to system frequencies ω and the cavity and atomic loss rates (κ, γ), one distinguishes several regimes [2]:

- **Weak coupling:** $g \ll \kappa, \gamma, \omega$. Light and matter interact perturbatively; spontaneous emission dominates.
- **Strong coupling:** $\kappa, \gamma \ll g \ll \omega$. Coherent exchange (vacuum Rabi oscillations) occurs before decay.
- **Ultrastrong coupling (USC):** $g/\omega \gtrsim 0.1$. The interaction strength is comparable to bare frequencies, causing non-perturbative effects and breakdown of the rotating-wave approximation.
- **Deep strong coupling (DSC):** $g/\omega \gtrsim 1$. Coupling dominates all energy scales; qualitatively new physics emerges.

2.3. Experimental Realizations

In recent decades, many experimental platforms have demonstrated different regimes of light–matter coupling [9, 10, 23–27]. Early experiments in cavity quantum electrodynamics (cQED) used atoms inside high-quality optical or microwave cavities [22, 27]. In 1983, Haroche and collaborators achieved strong coupling by placing Rydberg atoms inside a microwave cavity and observing vacuum Rabi oscillations, which are a clear signature of coherent energy exchange between light and matter [23].

A few years later, strong coupling was also reached with single atoms in both microwave [25] and optical cavities [24]. In 1992, strong coupling was demonstrated in solid-state systems, where excitons in semiconductor quantum wells interacted with optical microcavities, forming so-called cavity polaritons [10].

More recently, artificial atoms, such as quantum dots and superconducting qubits, have been coupled to resonators to study light-matter interactions. In particular, superconducting circuits (circuit QED) have made it possible to reach the ultrastrong coupling regime. In 2010, Niemczyk *et al.* [9] observed a normalized coupling strength of $g/\omega \approx 0.12$ between a superconducting qubit and a microwave resonator, which in this setup plays the role of the light mode, placing the system clearly in the USC regime.

Another important class of experiments involves semiconductor quantum wells embedded in optical cavities. In 2009, Günter *et al.* [26] showed that many electrons in a doped GaAs quantum well can collectively couple to light strongly enough to enter the USC regime, with a coupling ratio of about $g/\omega \approx 0.11$.

These examples show that USC is not limited to one specific system. It has now been observed in various platforms, including molecules [28], plasmonic structures [29], and vibrational modes in solids [30]. This broad range of implementations highlights the general relevance of USC and motivates the development of simplified theoretical models to gain a deeper understanding of this physics.

2.4. The Dicke Model

To understand the collective behavior observed in many experiments with strong light-matter coupling, it is useful to consider simplified but physically motivated models. One of the most prominent examples is the Dicke model [3], which describes N identical two-level

systems (often referred to as atoms or qubits) coupled to a single mode of the quantized electromagnetic field.

The Dicke Hamiltonian captures essential features of cQED systems and is particularly relevant in the strong and ultrastrong coupling regimes, since in these regimes the rotating-wave approximation breaks down and the counter-rotating terms play a crucial role. It is typically derived starting from the minimal coupling Hamiltonian in the Coulomb gauge, where charged particles interact with the quantized vector potential $\hat{\mathbf{A}}$. For a system of N two-level emitters, the interaction Hamiltonian reads:

$$\hat{H} = \sum_{j=1}^{N} \left[\frac{1}{2m} \left(\hat{\mathbf{p}}_j - q\hat{\mathbf{A}} \right)^2 + V(\hat{\mathbf{r}}_j) \right] + \hat{H}_{\text{field}} \,. \tag{1}$$

Expanding the square yields three terms: the kinetic energy ($\propto \mathbf{p}^2$), the paramagnetic coupling ($\propto \hat{\mathbf{p}} \cdot \hat{\mathbf{A}}$), and the diamagnetic term ($\propto \hat{\mathbf{A}}^2$). After performing the dipole approximation and restricting the system to two-levels, the interaction can be expressed in terms of Pauli operators and a bosonic mode with creation (annihilation) operator $\hat{a}^\dagger$ ($\hat{a}$). This leads to the Dicke Hamiltonian [2]:

$$\hat{H}_{\text{Dicke}+A^2} = \omega_c \hat{a}^\dagger \hat{a} + 2\varepsilon \hat{S}_z + \frac{g}{\sqrt{N}} \left(\hat{a}^\dagger + \hat{a} \right) \hat{S}_x + D \left(\hat{a}^\dagger + \hat{a} \right)^2 . \tag{2}$$

The interaction term of strength $g/\sqrt{N}$ ensures a well-defined thermodynamic limit as $N \to \infty$, where N is the number of two-level systems. The collective spin operators are defined as $\hat{S}_\alpha = \sum_i \frac{\sigma_i^\alpha}{2}$, for $\alpha \in \{x, y, z\}$ and the Pauli matrices σ_i^α. They satisfy the SU(2) commutation relations

$$\left[\hat{S}_\alpha, \hat{S}_\beta \right] = \mathrm{i} \varepsilon_{\alpha\beta\gamma} \hat{S}_\gamma \tag{3}$$

and the bosonic operators $\hat{a}^\dagger$ and $\hat{a}$ obey the canonical commutation relation

$$\left[\hat{a}, \hat{a}^\dagger \right] = 1 \,. \tag{4}$$

The first three terms define the standard Dicke model, while the last term, proportional to $\left(\hat{a}^\dagger + \hat{a}\right)^2$, originates from the diamagnetic A^2 contribution. Its prefactor D quantifies the strength of this contribution. Although it is often neglected in theoretical treatments, the A^2 term becomes essential in the ultrastrong coupling regime and plays a crucial role in certain so-called no-go theorem for superradiant phase transitions [6–8].

In what follows, we will focus first on the Dicke model without the A^2 term to explore its physical predictions, and later comment on the implications of including this diamagnetic contribution.

The standard Dicke model is defined as

$$\hat{\mathcal{H}}_{\text{Dicke}} = \omega_c \hat{a}^\dagger \hat{a} + 2\varepsilon \hat{S}_z + \frac{g}{\sqrt{N}} \left(\hat{a}^\dagger + \hat{a}\right) \hat{S}_x \,, \tag{5}$$

where ε denotes the energy difference between the two (spin) levels of $\hat{S}_z$, and ω_c is the frequency of the cavity mode.

The Dicke model possesses a discrete $\mathbb{Z}_2$ parity symmetry, under which the transformation $(\hat{a}, \hat{S}_x) \to (-\hat{a}, -\hat{S}_x)$ leaves the Hamiltonian invariant. This symmetry corresponds to the conservation of excitation parity. The system is said to be in the normal phase when this symmetry is preserved and in the superradiant phase when it is spontaneously broken.

The presence of a phase transition in the Dicke model was rigorously established in the thermodynamic limit by Hepp and Lieb [4], as well as by Wang and Hioe [5]. The transition can be analyzed via a mean-field approach, which becomes exact as $N \to \infty$. At thermal equilibrium, the critical coupling strength g_c is found by minimizing the mean-field free energy, resulting in

$$g_c = \sqrt{2\varepsilon\omega_c \coth\left(\frac{2\varepsilon}{2T}\right)} \,, \tag{6}$$

where T is the temperature. In the zero-temperature limit $T \to 0$, the model exhibits a quantum phase transition at

$$g_c = \sqrt{2\varepsilon\omega_c} \,. \tag{7}$$

A related model, the Tavis–Cummings model, is obtained by applying the rotating-wave approximation (RWA) to the Dicke Hamiltonian. This approximation neglects the counter-rotating terms, leading to a model that conserves the total number of excitations and possesses a continuous $U(1)$ symmetry. The Tavis–Cummings model does not exhibit a thermal phase transition in equilibrium [1, 31].

In contrast to light–matter Hamiltonians, where collective behavior emerges from the coupling of spins to bosonic modes, one can also capture collective phenomena by considering direct interactions between spins themselves, which we discuss next.

2.5. The Ising model

The Ising model is one of the most fundamental and widely studied models in statistical and condensed matter physics. Originally introduced by Wilhelm Lenz and solved in one dimension by his student Ernst Ising [32], the model captures essential features of cooperative phenomena such as ferromagnetism and phase transitions.

In its classical form, the Ising model consists of binary spin variables $\sigma_i = \pm 1$ placed on the sites of a lattice, with only nearest-neighbor interactions. The Hamiltonian of the Ising model is given by

$$H_{\text{Ising}} = -J \sum_{\langle i,j \rangle} \sigma_i \sigma_j \,, \tag{8}$$

where the parameter J sets the interaction strength. For $J > 0$, the system favors ferromagnetic alignment, while $J < 0$ corresponds to antiferromagnetic interactions. The sum $\langle i, j \rangle$ runs over all nearest-neighbor pairs on the lattice.

A key feature of the Ising model is its global $\mathbb{Z}_2$ symmetry: the Hamiltonian remains invariant under the transformation $\sum_i \sigma_i \to \sum_i -\sigma_i$. This symmetry reflects the physical equivalence of the two magnetized states and is spontaneously broken in the ordered phase of the system. At high temperatures, thermal fluctuations dominate and the system is disordered with zero net magnetization, where the magnetization operator is defined as $\hat{M} = \sum_j \hat{\sigma}_j^z$. Below a critical temperature T_c, the system enters a ferromagnetic phase where the $\mathbb{Z}_2$ symmetry is spontaneously broken, and the magnetization acquires a non-zero expectation value.

While the one-dimensional model does not exhibit a phase transition at any finite temperature, the two-dimensional Ising model on a square lattice was famously solved exactly by Lars Onsager in 1944 [33]. He showed that it exhibits a continuous (second-order) phase transition for ferromagnetic interactions at a finite critical temperature.

$$T_c = \frac{2J}{\ln(1 + \sqrt{2})} \,.$$

This result was one of the first exact demonstrations of a phase transition in a lattice model and is a cornerstone of statistical mechanics.

A quantum extension of the Ising model, known as the transverse-field Ising model (TFIM), introduces quantum fluctuations via a transverse magnetic field. The Hamiltonian in one

dimension is as

$$H_{\mathrm{TFIM}} = -J \sum_i \sigma_i^z \sigma_{i+1}^z - h \sum_i \sigma_i^x \,, \tag{9}$$

where σ_i^α are Pauli matrices acting on spin-$\frac{1}{2}$ degrees of freedom, and h is the transverse field strength. This model also respects a global $\mathbb{Z}_2$ symmetry, generated by the operator $\prod_i \sigma_i^x$, which flips all spins in the z-direction. As in the classical case, this symmetry can be spontaneously broken in the ordered phase.

The TFIM undergoes a quantum phase transition at zero temperature when the transverse field reaches a critical value $h_c = J$ [34]. For $h < h_c$, the system is in an ordered ferromagnetic phase with broken symmetry; for $h > h_c$, quantum fluctuations destroy this long-range order, leading to a symmetric paramagnetic phase. The same picture holds in the antiferromagnetic case, where an ordered Néel phase gives way to the paramagnet at the critical field. This transition is a paradigmatic example of a quantum phase transition driven by quantum, rather than thermal, fluctuations.

In addition to its foundational role in statistical physics, the Ising model has gained relevance in statistical inference [35] and machine learning [36]. Its Boltzmann distribution defines a probability measure over binary variables, and the so-called inverse Ising problem—inferring [37] the couplings J_{ij} from observed data—has found applications in neuroscience, biology, and information theory [38]. In this sense, the Ising model serves as a bridge between equilibrium statistical mechanics and modern data-driven sciences.

2.6. Dicke-Ising Model

The Dicke–Ising model extends the Dicke model by incorporating direct interactions between the matter degrees of freedom. Concretely, it serves as a minimal model to study both light–matter and matter–matter interactions, obtained by adding a nearest-neighbor Ising interaction between the N spin-$\frac{1}{2}$ to the standard Dicke Hamiltonian. The Hamiltonian is given as

$$\hat{\mathcal{H}}_{\mathrm{DIM}} = 2\varepsilon \hat{S}_z + \frac{g}{\sqrt{N}}(\hat{a}^\dagger + \hat{a})\hat{S}_x + \omega_c \hat{a}^\dagger \hat{a} - J \sum_{\langle i,j \rangle} \sigma_i^z \sigma_j^z \,. \tag{10}$$

For $2\varepsilon = 0$ the model possesses a $\mathbb{Z}_2 \times \mathbb{Z}_2$ symmetry, inherited from the Dicke and the Ising model. For a finite longitudinal field $2\varepsilon \neq 0$ for ferromagnetic Ising interactions ($J > 0$) one $\mathbb{Z}_2$ symmetry is broken. For antiferromagnetic Ising interactions ($J < 0$), the relevant

symmetry is still $\mathbb{Z}_2 \times \mathbb{Z}_2$. Although the longitudinal field explicitly breaks the spin-flip symmetry, also in the AF case, here the translation symmetry can be spontaneously broken, which for $\varepsilon = 0$ is equivalent to the spin-flip symmetry.

The zero-temperature properties of the model in 1D have been studied using mean-field theory [14, 39] as well as quantum Monte Carlo (QMC) simulations, both within the rotating-wave approximation (RWA) [40] and for the full model [18]. Rohn *et al.* [15] analytically demonstrated that the quantum phase transition at $\varepsilon = 0$ is of first order. Using QMC with the wormhole algorithm, this result was later shown to remain also at finite ε on both the one-dimensional chain and the square lattice [18], in contrast to the second-order prediction of mean-field theory for any finite ε.

2.6.1. Phase diagram of the Dicke-Ising model

We present the mean-field phase diagram together with the numerically obtained quantitative Quantum Monte Carlo simulations (QMC) results for the one-dimensional Dicke-Ising model. The phase diagram is visualized in terms of the spin-photon coupling g/ω_c and the Ising interaction strength J/ω_c, for a fixed longitudinal field $\varepsilon/\omega_c = 0.3$. This allows for a unified comparison of ferromagnetic ($J < 0$) and antiferromagnetic ($J > 0$) regimes within a single framework.

As shown in Fig. 1, the mean-field analysis predicts four distinct phases: the paramagnetic normal phase (PN), the paramagnetic superradiant phase (PS), the antiferromagnetic normal phase (AN), and the antiferromagnetic superradiant phase (AS). The AS phase is particularly noteworthy as it features simultaneous spin and photonic order, thereby breaking both spin-flip and parity symmetries.

For ferromagnetic interactions ($J < 0$), for small longitudinal fields the quantum phase transition remains first-order, in contrast to the immediate second-order behavior predicted by mean-field theory. In the antiferromagnetic regime, the AS phase remains robust, but in the one-dimensional case, the intermediate AS phase is very small in the parameter space as shown in Fig. 1.

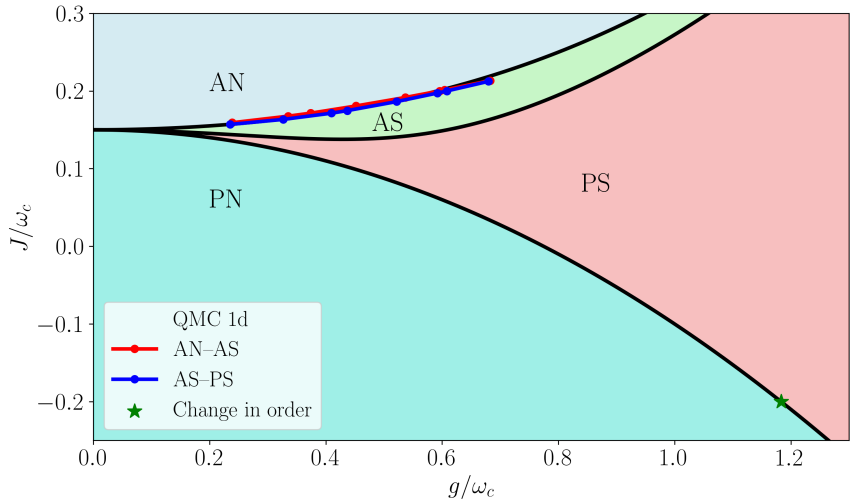

Figure 1: Mean-field phase diagram of the Dicke-Ising model at fixed longitudinal field $\varepsilon/\omega_c = 0.3$, plotted as a function of spin-photon coupling g/ω_c and Ising interaction strength J/ω_c. Four phases are identified: paramagnetic normal (PN), paramagnetic superradiant (PS), antiferromagnetic normal (AN), and antiferromagnetic superradiant (AS). The AS phase breaks both $\mathbb{Z}_2$ symmetries and emerges only for antiferromagnetic couplings. Additionally, the QMC results [41] for 1D are shown in colored lines. They illustrate how narrow the intermediate AS phase is in 1D and how the order of the phase transition changes for ferromagnetic interactions.

2.6.2. Influence of the diamagnetic A^2-term on the Dicke–Ising model

In addition to its role in the standard Dicke model Equation 5, the diamagnetic A^2-term also plays an important part in the extended Dicke-Ising model. This term naturally arises when the microscopic light–matter coupling is derived via the minimal coupling substitution in the Coulomb gauge as shown before. It takes the form

$$\hat{H}_{A^2} = D\left(\hat{a}^\dagger + \hat{a}\right)^2, \tag{11}$$

where D quantifies the strength of the diamagnetic interaction. In the limiting case of vanishing spin–spin interactions ($J = 0$), this term is known to suppress the superradiant phase transition [6].

Within the Dicke-Ising framework, the A^2-term can be effectively absorbed into a redefinition of the photon frequency and coupling strength using a Bogoliubov transformation [2, 18].

This results in renormalized parameters

$$\omega' = \sqrt{\omega^2 + 4\omega D}\,, \tag{12}$$

$$g' = \sqrt{\frac{\omega}{\omega'}}\, g\,, \tag{13}$$

where ω' is the renormalized photon frequency and g' the effective light–matter coupling. The value of D is not independent: the Thomas-Reiche-Kuhn (TRK) sum rule imposes a lower bound $D \geq g^2/2\varepsilon$, where ε is the transition energy of the two-level system [8].

Despite the presence of this additional term, Quantum Monte Carlo (QMC) simulations have shown that the rich phase structure of the Dicke–Ising model is preserved for antiferromagnetic Ising interactions [18], given that the same lower bound for D holds as for the Dicke model. However, in the case of ferromagnetic spin-spin coupling, the diamagnetic term suppresses the superradiant phase, consistent with no-go theorems from cavity QED.

2.7. Self-Consistent Effective matter Hamiltonian

It is possible to derive an effective matter Hamiltonian for the Dicke-Ising model in the ultrastrong coupling limit. This can be achieved by applying a displacement transformation to the Hamiltonian, followed by a mean-field decoupling.

2.7.1. Displacement transformation

In order to make the calculations easier, the Hamiltonian is transformed as in [15] with a displacement operator $\hat{D}(\alpha) \coloneqq \exp\left[\alpha \hat{S}_x \left(\hat{a}^\dagger - \hat{a}\right)\right]$, where $\alpha \coloneqq \frac{g}{\omega_c \sqrt{N}}$. This unitary operator has the ability to displace a vacuum state $|0\rangle$ into a coherent state $|\alpha\rangle$ in the photon subspace $\hat{S}_x |\alpha\rangle = \hat{D}(\alpha)|0\rangle$ with an amplitude depending on the value of the $\hat{S}_x$ operator, which lives in the Hilbert space of the spins. A coherent state is defined as an eigenstate of the annihilation operator $\hat{a}$

$$\hat{a}\,|\alpha\rangle = \alpha\,|\alpha\rangle\ . \tag{14}$$

For the case $2\varepsilon = 0$, the displacement transformation makes the problem trivial because it diagonalizes the Hamiltonian [15]. The effect of the displacement transformation on the

ladder operators can be easily calculated with the Baker-Campbell-Hausdorff-Formula

$$e^{\hat{A}}\hat{B}e^{-\hat{A}} = \sum_{m=0}^{\infty} \frac{1}{m!}\left[\hat{A},\hat{B}\right]_m , \tag{15}$$

$$\text{with } \left[\hat{A},\hat{B}\right]_m = \left[A,\left[\hat{A},\hat{B}\right]_{m-1}\right] \text{ and } \left[\hat{A},\hat{B}\right]_0 = \hat{B} . \tag{16}$$

The result is

$$\hat{D}^\dagger \hat{a} \hat{D} = \hat{a} + \alpha \hat{S}_x, \tag{17}$$

$$\hat{D}^\dagger \hat{a}^\dagger \hat{D} = \hat{a}^\dagger + \alpha \hat{S}_x . \tag{18}$$

This means, the displacement transformation shifts the ladder operators by $\alpha\hat{S}_x$. After that, the only missing part to transform the whole Hamiltonian is the action of the displacement operator on the Pauli z matrix and the product of two Pauli z matrices. This calculation is straightforward using the Baker-Campbell-Hausdorff-Formula and the two commutation relations

$$\left[\frac{\sum_i \sigma_i^x}{2}, \sum_j \sigma_j^z\right]_m = \begin{cases} \sum_i -i\sigma_i^y , & \text{m odd} \\ \sum_i \sigma_i^z , & \text{m even} \end{cases} \tag{19}$$

and

$$\left[\frac{\sum_i \sigma_i^x}{2}, \sum_j \sigma_j^z \sigma_{j+1}^z\right]_m = \begin{cases} -2^m i\,(yz + zy) , & \text{m odd} \\ 2^m\,(zz - yy) & \text{m even} \end{cases} . \tag{20}$$

Here we introduced the notation $\gamma\delta \coloneqq \sum_i \sigma_i^\gamma \sigma_{i+1}^\delta$ and in the following $\hat{r} := \alpha\left(\hat{a}^\dagger - \hat{a}\right)$ is used. With the help of the above derived identities, the Hamiltonian can be displaced and reads [15]

$$\begin{aligned} \hat{\mathcal{H}} = \hat{D}\hat{\mathcal{H}}_{\text{DIM}}\hat{D}^\dagger = &- J\left[zz + \frac{1}{2}(zz - yy)(\cosh 2\hat{r} - \mathbb{1}) - \frac{i}{2}(yz + zy)\sinh 2\hat{r}\right] \\ &+ 2\varepsilon\left[\hat{S}_z \cosh\hat{r} - i\hat{S}_y \sinh\hat{r}\right] + \omega_c\left[\hat{a}^\dagger\hat{a} - \alpha^2\hat{S}_x^2\right] . \end{aligned} \tag{21}$$

In the regime of interest, namely the *superradiant regime*, the displacement parameter α remains small. This follows because we are working in the thermodynamic limit, where the photon field expectation value scales with the system size and the effective expansion parameter becomes suppressed. As discussed by Rohn *et al.* [15], this allows one to write the

Hamiltonian in this regime as

$$\hat{\mathcal{H}} = \omega_c \hat{a}^\dagger \hat{a} - \frac{g^2}{\omega_c N} \hat{S}_x^2 + 2\varepsilon \hat{S}_z - J \sum_{\langle i,j \rangle} \sigma_i^z \sigma_j^z \,. \tag{22}$$

In fact, various independent approaches have confirmed that in the thermodynamic limit the Dicke model's collective atomic degrees of freedom become equivalent to those of the Lipkin–Meshkov–Glick (LMG) model. For example, Brankov *et al.* [42] and Gibberd [43] rigorously mapped the Dicke Hamiltonian onto an infinite-range spin model (equivalent to the LMG model) in the limit of infinitely many atoms. Using a Holstein–Primakoff transformation and finite-size scaling analysis, Vidal and Dusuel [44] showed that the Dicke model's critical scaling exponents for atomic observables coincide with those of the LMG model. Similarly, Reslen *et al.* [45] employed entanglement-scaling techniques and derived an effective spin Hamiltonian for the atomic subsystem, demonstrating that the Dicke quantum phase transition falls into the same universality class as an infinite-range (LMG-type) spin model. In addition, a high-temperature expansion of the Dicke model's partition function by Liberti and Zaffino [46] showed that the Dicke model in the strong-coupling regime can be connected to a collective one-dimensional Ising model of LMG type. Taken together, these diverse methods consistently indicate that in the large-N limit the Dicke model's atomic sector behaves identically to the LMG model, yielding the same critical behavior and phase-transition characteristics.

For $\gamma = 0$ the LMG Hamiltonian takes the form

$$\hat{H}_{\mathrm{LMG}} = -\frac{\lambda}{N} \hat{S}_x^2 - h \hat{S}_z \,, \tag{23}$$

which serves as the effective atomic description of the Dicke model in the thermodynamic limit. By contrast, our effective Hamiltonian in Eq. (22) contains in addition a nearest-neighbor Ising coupling term $-J \sum_{\langle i,j \rangle} \sigma_i^z \sigma_j^z$. Under the displacement transformation this term generates photon-dependent corrections, but these scale only subextensively with N and therefore vanish in the thermodynamic limit. As a result, the Ising coupling persists unchanged in Eq. (22), enriching the phase diagram beyond the pure Dicke–LMG correspondence.

2.7.2. Mean-field decoupling

The last step applied to the model is a mean-field decoupling on $\hat{S}_x^2$. Within this approach, the model reduces to a spin system featuring solely nearest-neighbor interactions while being coupled to a mean field. Therefore, light and matter can be considered separately. This gives a simpler Hamiltonian that can be investigated. The decoupling can be performed by expressing $\hat{S}_x$ by its mean value plus its fluctuation

$$\hat{S}_x = \langle \hat{S}_x \rangle + \delta \hat{S}_x \,. \tag{24}$$

By looking at the square of $\hat{S}_x$, the term $\delta \hat{S}_x^2$ is neglected

$$\begin{aligned} \hat{S}_x^2 &= \langle \hat{S}_x \rangle^2 + 2\langle \hat{S}_x \rangle \delta \hat{S}_x + \delta \hat{S}_x^2 \approx \langle \hat{S}_x \rangle^2 + 2\langle \hat{S}_x \rangle \delta \hat{S}_x \\ &= \langle \hat{S}_x \rangle (\langle \hat{S}_x \rangle + 2\delta \hat{S}_x) \overset{(24)}{=} \langle \hat{S}_x \rangle (\langle \hat{S}_x \rangle + 2\hat{S}_x - 2\langle \hat{S}_x \rangle) \\ &= \langle \hat{S}_x \rangle (2\hat{S}_x - \langle \hat{S}_x \rangle) = -\langle \hat{S}_x \rangle^2 + 2\langle \hat{S}_x \rangle \hat{S}_x \,. \end{aligned}$$

The expectation value of $\hat{S}_x$ is defined as the magnetization $M_x \equiv \langle \hat{S}_x \rangle$

$$\hat{S}_x^2 \approx -M_x^2 + 2M_x \hat{S}_x \,. \tag{25}$$

Inserting Equation 25 into Equation 22 yields the decoupled Hamiltonian

$$\hat{\mathcal{H}}_{\text{eff}}(m_x) = \frac{g^2 N}{\omega_c} m_x^2 + \omega_c \hat{a}^\dagger \hat{a} - \frac{g^2}{\omega_c} m_x \sum_i \sigma_i^x - J \sum_{\langle i,j \rangle} \sigma_i^z \sigma_j^z + \varepsilon \sum_i \sigma_i^z \tag{26}$$

with the magnetization per site $m_x = \frac{M_x}{N}$.

This is a self-consistent Hamiltonian, and its ground-state properties can be analyzed by investigating a transverse Ising model with a self-consistent transverse field and an additional longitudinal field. This is justified since the term $\omega_c \hat{a}^\dagger \hat{a}$ reaches its minimum at zero, and therefore vanishes in the ground state. Furthermore, the system has been rotated around the y-axis for convenience. This gives

$$\hat{\mathcal{H}}\,(m_z) = -2m_z \sum_i \sigma_i^z + J \sum_{\langle i,j \rangle} \sigma_i^x \sigma_j^x + \varepsilon \sum_i \sigma_i^x \,. \tag{27}$$

To obtain the ground-state energy, one solves Equation 27 self-consistently and then adds the term $\frac{g^2 N}{\omega_c} m_z^2$.

3. Methods

3.1. Non-Perturbative Linked-Cluster Expansion

The *Numerical Linked Cluster Expansion* (NLCE) provides a framework to compute extensive quantities directly in the thermodynamic limit by systematically summing contributions from finite, connected clusters of the system. An observable $\mathcal{M}$ is called *cluster-additive* if, for two disconnected clusters A and B, one has

$$\mathcal{M}(A \cup B) = \mathcal{M}(A) + \mathcal{M}(B)\,. \tag{28}$$

This property ensures that contributions from disconnected subclusters cancel when summing up contributions.

To avoid overcounting processes already present in smaller clusters, one introduces the *reduced contribution* $\widetilde{\mathcal{M}}(C)$ of a connected cluster C via the recursive definition

$$\widetilde{\mathcal{M}}(C) = \mathcal{M}(C) - \sum_{C' \subset C} \widetilde{\mathcal{M}}(C')\,, \tag{29}$$

where the sum runs over all connected proper subclusters $C' \subset C$. By construction, $\widetilde{\mathcal{M}}(C)$ isolates the part of $\mathcal{M}(C)$ arising from correlations involving all sites of C.

The corresponding intensive quantity of $\mathcal{M}$ is then obtained by summing the reduced contributions of all connected clusters, weighted by their number of embeddings per site in the infinite lattice. In practice, the sum is truncated at a maximum cluster size N, so that correlations up to size N are taken into account.

Simplification in one dimension. In one dimension, the cluster geometry simplifies drastically: up to translation, there is only one connected cluster of each size N, namely the chain C_N of N sites. For an open chain C_N, a connected subcluster of size i can be embedded in exactly $a_i = N - i + 1$ distinct ways, where a_i denotes the embedding factor [47].

For C_{N+1}, the corresponding factor is $b_i = N - i + 2$.

Starting from Equation 29 for C_{N+1}, we write

$$\widetilde{\mathcal{M}}(C_{N+1}) = \mathcal{M}(C_{N+1}) - \sum_{i=1}^{N} b_i \, \widetilde{\mathcal{M}}(C_i)\,, \tag{30}$$

and for C_N,

$$\widetilde{\mathcal{M}}(C_N) = \mathcal{M}(C_N) - \sum_{i=1}^{N-1} a_i \, \widetilde{\mathcal{M}}(C_i)\,. \tag{31}$$

Subtracting these two equations and using $b_i - a_i = 1$ for $i \leq N-1$ yields

$$\widetilde{\mathcal{M}}(C_{N+1}) - \widetilde{\mathcal{M}}(C_N) = \mathcal{M}(C_{N+1}) - \mathcal{M}(C_N) - \sum_{i=1}^{N-1} \widetilde{\mathcal{M}}(C_i) - 2\,\widetilde{\mathcal{M}}(C_N)\,. \tag{32}$$

Summing $\widetilde{\mathcal{M}}(C_i)$ over all clusters up to size $N+1$ and simplifying leads to

$$\mathcal{M}(\mathcal{L}_\infty) = \sum_{i=1}^{N+1} \widetilde{\mathcal{M}}(C_i) = \mathcal{M}(C_{N+1}) - \mathcal{M}(C_N)\,, \tag{33}$$

which is the compact 1D NLCE formula.

For the ground-state energy E_0, we thus obtain

$$e_0^{(N)} = E_0(C_N) - E_0(C_{N-1})\,, \tag{34}$$

where $e_0^{(N)}$ is the NLCE estimate of the energy per site in the thermodynamic limit using clusters up to size N. Here, $E_0(C_N)$ and $E_0(C_{N-1})$ denote the ground-state energies of open chains of length N and $N-1$, respectively.

Equation 34 isolates the net contribution of processes of range N, while all shorter-range processes cancel. By increasing N, one systematically incorporates longer-range correlations. For systems with finite correlation length, $e_0^{(N)}$ converges rapidly to the true ground-state energy density e_0 of the infinite chain. This telescoping form is a special feature of one-dimensional systems and does not directly generalize to higher dimensions, where the subtraction in Equation 29 involves many subclusters.

3.2. Exact Diagonalization

Exact diagonalization (ED) is a numerical method often used to study small quantum spin systems. It is especially helpful for understanding low-energy behavior and phase transitions [48, 49]. In this method, the Hamiltonian is written as a matrix and then exactly diagonalized to get all energy levels and corresponding states. Because it gives numerically exact results, ED is often used to check the accuracy and validity of other methods.

The main drawback of ED is that the size of the Hilbert space grows exponentially with the number of spins. This limits calculations to relatively small systems. To reduce boundary effects and better approximate large systems, periodic boundary conditions (PBC) are often employed, as they make the system behave more like an infinite one. Open boundary conditions (OBC), on the other hand, are necessary for calculating finite clusters in NLCE, which provides a better estimate of the thermodynamic limit than clusters of the same size with PBC.

In this thesis, ED calculation were performed using the QuSpin library [50, 51], a Python package made for quantum many-body problems. QuSpin makes it easy to define different lattices, custom Hamiltonians, and use system symmetries like translation, reflection, or spin flip. These symmetries help simplify the problem and reduce the size of the matrices, making it possible to study larger systems than with basic ED.

3.3. Density Matrix Renormalization Group

To study ground states and observables of quantum spin systems, we also used the Density Matrix Renormalization Group (DMRG) method. Introduced by White [52], DMRG is well known for giving very accurate ground state results for 1D quantum systems. It works by using Matrix Product States (MPS), which are an efficient way to represent quantum states in systems with low entanglement [53]. Because of this, DMRG is one of the standard tools for studying 1D quantum systems.

All DMRG calculations in this work were performed using the ITensor library [54], which is designed for tensor network methods. ITensor handles the technical parts of tensor operations and makes it easier to implement complex models. The simulations used open boundary conditions to improve efficiency and keep numerical costs low while still achieving accurate results.

We carefully checked that the DMRG results are well converged. This was done by looking at how much the ground-state energy changed between DMRG sweeps. Other quantities like truncation error and discarded weight were also monitored to make sure the results were reliable. Typical truncation errors were below 10^{-10}, showing very good accuracy. More details on convergence criteria are given in Appendix A.

To reduce finite-size effects, the DMRG results from small systems were combined with the NLCE method, as explained in subsection 3.1. Using DMRG together with NLCE gives accurate and reliable estimates for the thermodynamic limit.

3.4. High-order series expansion

High-order series expansion is a versatile analytical technique for studying quantum many-body systems in regimes where a small perturbative parameter exists. It enables the systematic approximation of physical quantities—such as the ground state energy, magnetization, or correlation functions—by expanding them in powers of the perturbation strength around an exactly solvable unperturbed limit in the thermodynmamic limit [55, 56].

The general starting point is a Hamiltonian of the form

$$H = H_0 + \lambda V \,, \tag{35}$$

where H_0 is exactly solvable, V is the perturbation, and $\lambda \ll 1$ is a small expansion parameter. Physical observables $Q(\lambda)$ are then written as a power series,

$$Q(\lambda) = Q^{(0)} + \lambda Q^{(1)} + \lambda^2 Q^{(2)} + \cdots + \lambda^n Q^{(n)} + \mathcal{O}(\lambda^{n+1}) \,, \tag{36}$$

with the coefficients $Q^{(k)}$ obtained perturbatively.

To extract quantities in the thermodynamic limit from such an expansion, we employ the *linked cluster expansion* (LCE), which builds the series from finite clusters of increasing size while eliminating disconnected or redundant subcluster contributions. For one-dimensional systems, the extensive part of a physical observable such as the ground-state energy can be extracted using the subtraction formula, similar to the one derived in subsection 3.1,

$$e_\infty(N) = E(N+n) - E(N) \,, \tag{37}$$

where $E(N)$ denotes the ground-state energy of a finite cluster with N sites, n is the number of sites in the unit cell of the lattice, and $e_\infty(N)$ provides an estimate of the thermodynamic limit. This factor n ensures consistency with the lattice geometry: for example, $n = 1$ for a simple chain, and $n = 2$ for the sawtooth chain with a two-site unit cell.

The result $E_\infty(N)$ is the quantity in the thermodynamic limit. One has to make sure that the desired order of the expansion fits on a cluster of size N to capture all relevant processes. The resulting series typically has a finite radius of convergence, particularly near phase transitions. To overcome this limitation and extend the reach of the expansion, we can make use of Padé and Dlog-Padé resummation techniques [57]. These approximants improve convergence and allow for analytic continuation, providing access to critical behavior such as singularities or phase boundaries.

In this work, we apply the high-order series expansion framework to both the unfrustrated linear chain and the geometrically frustrated sawtooth chain, enabling a comparative study of their ground-state properties and quantum phase transitions.

4. Multicritical Point in the Ferromagnetic Dicke-Ising chain

The ferromagnetic Dicke-Ising chain is interesting because the *order* of the quantum phase transition changes as the system parameters are varied. In the limit $J = 0$, the system reduces to the standard Dicke model, which exhibits a continuous (second-order) quantum phase transition with Dicke criticality [4]. In contrast, for $\varepsilon = 0$ the model becomes the quantized transverse-field Ising model (QTFIM), which undergoes a *first-order* quantum phase transition [15], with the exact transition point given in Appendix B. As discussed previously, the transition remains first order even in the presence of a small but finite longitudinal field [18].

Our aim is to determine with high precision the multicritical point, characterized by the coordinates $(J(g,\omega), \varepsilon(g,\omega))$, at which the transition changes from first to second order. Quantum Monte Carlo (QMC) simulations have provided a rough estimate of $J \approx \varepsilon$ for this point [18]. In the present work, we refine this estimate by combining the numerical linked-cluster expansion (NLCE) with density-matrix renormalization group (DMRG) calculations. As described in subsection 3.1, for the 1D chain the NLCE requires only two cluster sizes, N and $N+1$, each of which we solve to high accuracy using DMRG.

4.1. Self-consistent solution for ferromagnetic Ising couplings

The effective Hamiltonian Equation 27 depends on the longitudinal magnetization m_z, which must be determined self-consistently in the thermodynamic limit. We initialize the self-consistency loop in the strong-coupling regime ($g \gg \max\{J, \omega_c, \varepsilon\}$), where the transverse magnetization is close to its maximum value of $1/2$, and use this as an initial guess for m_z. In each iteration, the output value of m_z from a DMRG calculation is reinserted into the Hamiltonian as the new input parameter, and the system is re-solved until the difference between input and output m_z falls below a convergence threshold.

To accelerate convergence, we employ Anderson-accelerated fixed-point iterations [58] with the help of the julia package FixedPointAcceleration.jl [59]. In addition, the MPS wavefunction from the previous step serves as the initial state for the next DMRG run, significantly reducing the number of DMRG sweeps, which are back-and-forth optimizations along the chain, required for convergence.

Once a converged solution is obtained for a given g, we continue by gradually lowering g,

always using the previously converged m_z and MPS as initial conditions. For each value of g, the ground state is obtained through several DMRG sweeps until convergence is reached. In this way, we trace the phase boundary efficiently from large values of g down to $g = 0$.

4.2. Determining the order of the quantum phase transition

To determine the order of the quantum phase transition, we compare our numerical ground-state energies to the mean-field prediction, which, although approximate in general, is known to yield exact results in certain regimes of the Dicke–Ising chain.

In the weak-coupling limit,

$$g \ll \min\{J, \omega_c, \varepsilon\}\,,$$

the photon field is negligible, the spins remain in their unperturbed configuration, and the photon occupation is zero. The ground-state energy per site is then

$$\frac{E_0}{N} = -\frac{Jc}{2} - \varepsilon\,, \tag{38}$$

where c is the lattice connectivity ($c = 2$ for a chain with periodic boundary conditions) [17].

Mean-field theory predicts a continuous transition at

$$g_{\mathrm{crit}} = \sqrt{2\varepsilon + 2cJ}\,. \tag{39}$$

The criterion for distinguishing first and second order is:

- **Second-order transition:**
  If the numerical ground-state energy at the mean-field critical point $g_{\mathrm{crit}}^{\mathrm{MF}}$ agrees with the mean-field value, the transition is continuous and therefore of second order.
- **First-order transition:**
  If the numerical ground-state energy at $g_{\mathrm{crit}}^{\mathrm{MF}}$ is lower than the mean-field prediction, another phase with smaller energy has already crossed in at a coupling $g < g_{\mathrm{crit}}^{\mathrm{MF}}$. This sharp level crossing signals a first-order transition.

This purely energy-based method is straightforward to implement and robust against finite-size effects, making it well suited for locating the multicritical point. We note, however, that this criterion assumes a direct competition between two phases. If additional intermediate

phases exist, as can occur in the Dicke–Ising model, the analysis must be refined by explicitly resolving which phase realizes the true ground state in the relevant coupling regime.

4.3. Examples: first- vs. second-order transitions

We first validate the method with two parameter sets deep in the first- and second-order regimes.

First-order example ($\varepsilon = 0.0$). Figure 2 shows the ground-state energy (a) and transverse magnetization (b) for $J = -0.2$ and $\varepsilon = 0.0$. Forward (*low*) and backward (*high*) sweeps in g produce distinct energy branches near the transition, crossing at a finite angle and displaying hysteresis, hallmarks of a first-order transition. The magnetization exhibits a clear discontinuous jump. The self-consistency is solved and confirms convergence.

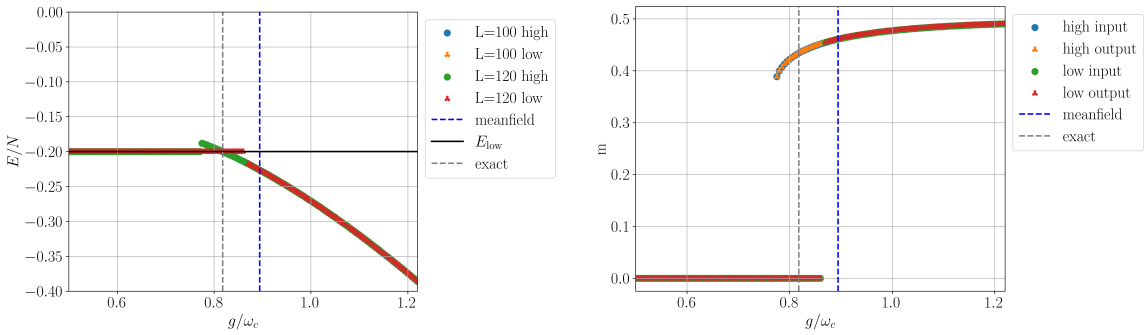

(a) Ground-state energy for $L = \{100, 120\}$ from high (decreasing g) and low (increasing g) sweeps. The absence of a smooth connection and the hysteresis are clear indicators of a first-order transition.

(b) Transverse magnetization for $L = 100$, showing a clear jump at the transition. Input refers to the m_z inserted into Equation 27, output to the measured ground-state value-indicating convergence of the self-consistency loop.

Figure 2: Example of a first-order quantum phase transition for $\varepsilon = 0.0$ and $J = -0.2$.

Second-order example ($\varepsilon = 0.5$). In Figure 3, energies from forward and backward sweeps coincide, and the transition point matches the mean-field prediction. The magnetization changes smoothly without a jump, indicating a second-order transition. Again, the self-consistency condition is satisfied to high accuracy.

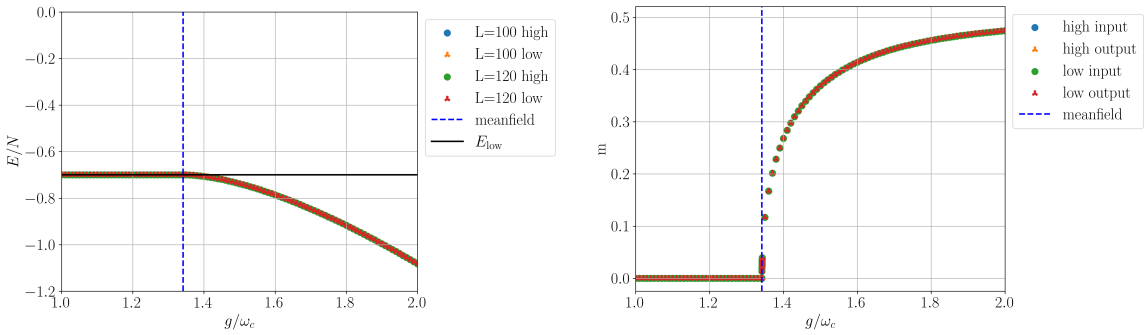

(a) Ground-state energy for $L = \{100, 120\}$, showing smooth connection between low and high sweeps and agreement with mean-field theory—consistent with a second-order transition.

(b) Transverse magnetization for $L = 100$, changing continuously without a jump. Self-consistency is again well satisfied.

Figure 3: Example of a second-order quantum phase transition for $\varepsilon = 0.5$ and $J = -0.2$.

4.4. Locating the multicritical point

Having validated the procedure, we now determine the multicritical point for $J = -0.2$. We sample g values around the mean-field prediction (39) for $\varepsilon/\omega_c \in [0.1, 0.3]$, motivated by the QMC estimate $\varepsilon \approx |J|$ [18]. For each ε, we compute

$$\Delta E = E_{\text{DMRG+NLCE}} - E_{\text{weak}} \,, \tag{40}$$

where $E_{\text{DMRG+NLCE}}$ is the self-consistent NLCE+DMRG energy from the large g limit and E_{weak} the exact weak-coupling energy.

In this formulation, ΔE does not change sign across the transition; instead, the transition order changes precisely at the point where ΔE becomes *zero*. As shown in Figure 4, this occurs at $\varepsilon/\omega_c = 0.200124$, in excellent agreement with the QMC estimate of $\varepsilon \approx |J|$. The high precision of this result reflects both the numerical accuracy of the DMRG calculations (relative energy errors below 10^{-9}, see Appendix A) and the precise control over the sampling in g.

Figure 5 summarizes the findings. The background shows the mean-field phase diagram for $J = -0.2$, while the points mark the numerically determined phase boundaries. Blue points correspond to second-order transitions, red points to first-order transitions. The point at $\varepsilon/\omega_c = 0.200124$ marks the multicritical point where the order changes.

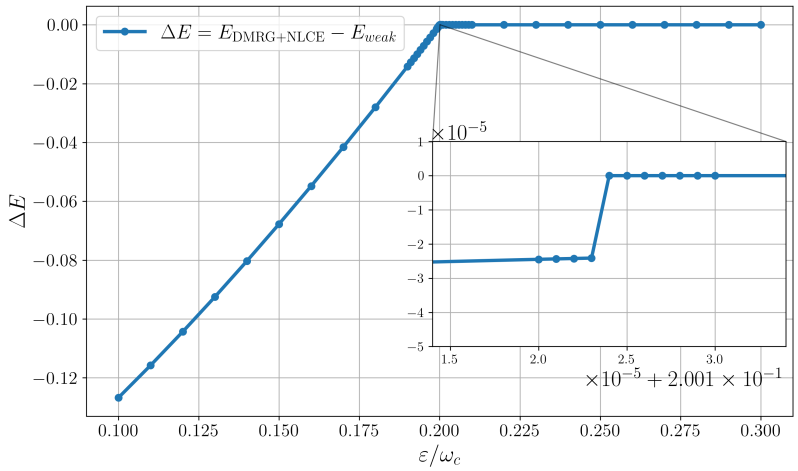

Figure 4: Difference between the calculated ground-state energy and the exact weak-coupling energy. The transition order changes from first to second precisely at the point where $\Delta E = 0$, here $\varepsilon/\omega_c = 0.200124$.

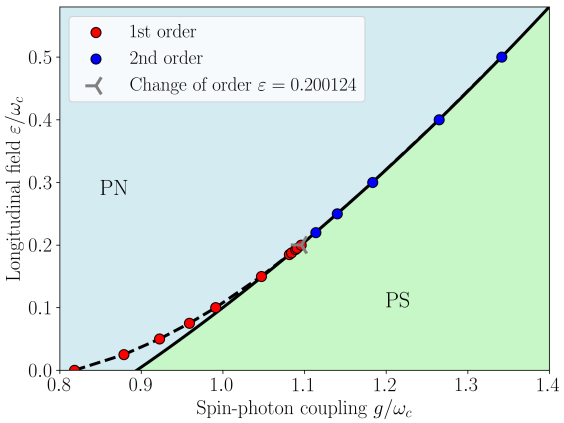

Figure 5: Mean-field phase diagram for $J = -0.2$ with numerically calculated phase boundaries from DMRG+NLCE. Blue points: second-order transitions; red points: first-order transitions. The multicritical point is located at $\varepsilon/\omega_c = 0.200124$.

5. Antiferromagnetic Superradiance in the Dicke-Ising chain

For the antferromagnetic Dicke-Ising chain we are particulary interested in the antiferromagnetic superradiant phase, which is characterized by the order in the matter and in the light degrees of freedom. This makes it hard to tackle the problem with a perturbative approach because there is no analytical solvable perturbative limit for this phase. However, our method which combines NLCE with DMRG does not need such a limit. To capture the antiferromagnetic order one needs to measure the staggered magnetization, which is defined as

$$m_{\mathrm{s}} = \frac{1}{2N} \sum_{i=1}^{N} (-1)^n \, \sigma_i^x \, . \tag{41}$$

The superradiant phase can be characterized by the transverse magnetization m_z, as in the ferromagnetic case discussed in subsection 4.1. To determine the phase boundaries, we perform adiabatic sweeps in the light–matter coupling g: one starting from large g and one from $g = 0$. In the case of a continuous (second-order) transition, both sweeps yield the same critical coupling. If the transition is of first order, however, hysteresis effects appear and the two sweeps lead to different results. In this situation, the critical value of g is defined by the intersection of the ground-state energies obtained from the two sweeps. Further modifications specific to the antiferromagnetic case will be introduced below.

5.1. Solving the self-consistency for antiferromagnetic Ising couplings

Due to the alternating spins in an antiferromagnetic configuration only even clusters are evaluated, since only then the desired staggered magnetization of 1/2 (Equation 41) corresponding to maximal antiferromagnetic order can be realized. To achieve this, we employ the NLCE formula Equation 34 using a two-site unit cell, consisting of one spin-up and one spin-down site. So, the formula changes to

$$e_0^{(N)} = E_0(C_N) - E_0(C_{N-2}) \, . \tag{42}$$

Furthermore, we need the staggered magnetization in x-direction to measure the antiferromagnetic order. To select the same orientation of the spins on both clusters of size N and $N + 2$, one has to introduce an environmental field to the first and last spin of the chains in x-direction of the form

$$\hat{\mathcal{H}}_{\mathrm{env}} = 2Jm_s\sigma_1^x - 2Jm_s\sigma_N^x \tag{43}$$

for the cluster of size N. For the cluster of size $N+2$ the second term is applied to the spin $N+2$. The field acts as a small external symmetry-breaking term, selecting one of the two degenerate Néel configurations and ensuring a consistent spin orientation between clusters of different size. The vanishing of the staggered magnetization m_s accounts for the fact that the antiferromagnetic order slowly gets destroyed in the intermediate phase until no antiferromagnetic order is present. The factor of 2 is necessary to have an environment field of J in the completely antiferromagnetic phase, where $m_s = 1/2$.

5.2. Results

To investigate the antiferromagnetic superradiant phase, we fix $J = 0.2$ and $\varepsilon = 0.3$, which allows for a direct comparison with QMC data from Ref. [18]. In this regime, the system exhibits three distinct phases: the *antiferromagnetic normal* (AN) phase, the *antiferromagnetic superradiant* (AS) phase, and the *paramagnetic superradiant* (PS) phase, as introduced in the previous sections. In addition to the adiabatic sweep starting from large g (high sweep), we also perform a sweep starting from small g (low sweep), where g is increased adiabatically. Comparing these two sweeps enables a clear identification of first-order phase transitions via the intersection points of the corresponding ground-state energy curves and through the appearance of hysteresis effects.

In Figure 6 we present the ground-state energy per site for $L = 70$ and $L = 100$ sites. The data for both system sizes agree very well, indicating fast convergence with respect to system size. The main panel shows the full range of g/ω_c, while the inset focuses on the transition region. The vertical dashed lines mark the phase boundaries between AN-AS (blue) and AS-PS (magenta).

The quantum phase transition from AN to AS occurs at $g_{\text{crit}} \approx 0.592$ and is continuous, consistent with a second-order transition. In contrast, the transition from AS to PS is clearly of first order: the low- and high-sweep curves cross at a finite angle, and each sweep remains in its metastable branch before abruptly switching to the energetically favored branch of the other phase. This hysteresis behavior is typical for first-order quantum phase transitions.

The behavior of the order parameters is shown in Figure 7. The transverse magnetization m_z (yellow) serves as the order parameter for superradiance, while the staggered magnetization m_s (purple) captures the antiferromagnetic ordering of the matter degrees of freedom.

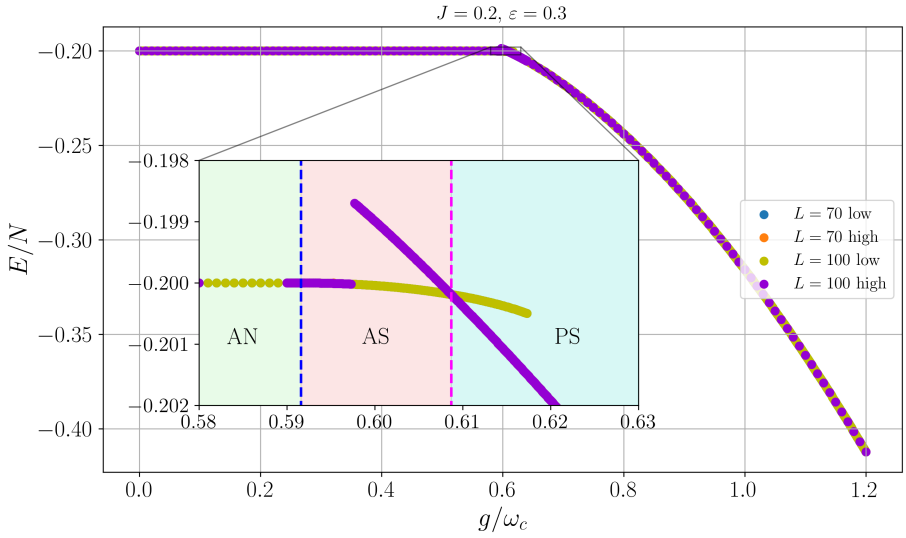

Figure 6: Ground-state energy per site for $J = 0.2$ and $\varepsilon = 0.3$ obtained from adiabatic sweeps starting from low (orange, yellow) and high (blue, purple) g for system sizes $L = \{70, 100\}$. The inset shows a zoom into the transition region with the AN-AS and AS-PS boundaries indicated by dashed lines. The hysteresis demonstrates the first-order nature of the AS–PS transition.

In the AN phase, m_s is maximal and m_z is zero, consistent with an antiferromagnetic spin arrangement with a vanishing photon density. In the PS phase on the right, m_s vanishes while m_z remains finite, indicating the absence of matter order but the presence of a macroscopic photon population. The intermediate AS phase in the middle is characterized by finite values of both m_s and m_z, signaling simultaneous antiferromagnetic order and superradiance.

The order parameters further confirm the order of the phase transitions. m_s and m_z change continuously at the AN-AS transition (second order), whereas both exhibit discontinuous jumps at the AS-PS boundary (first order).

It should be noted, however, that our approach can face difficulties in the presence of two consecutive first-order transitions. In such a situation, the hysteresis inherent to each transition may overlap, making it hard to unambiguously identify both critical couplings. As a result, distinguishing the two phase boundaries becomes less reliable compared to the case of a single first-order transition.

Overall, our method allows for a precise identification of the intermediate antiferromagnetic superradiant phase, including accurate determination of its phase boundaries and the charac-

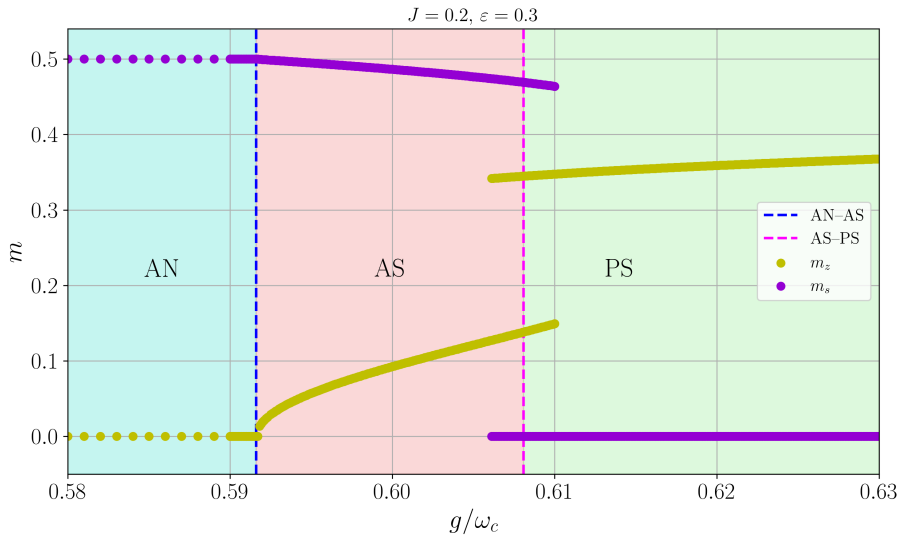

Figure 7: Order parameters m_z (yellow) and m_s (purple) as a function of g/ω_c for $J = 0.2$ and $\varepsilon = 0.3$. The vertical dashed lines mark the AN–AS and AS–PS phase boundaries. The shaded regions indicate the three phases: AN (cyan), AS (red), and PS (green).

terization of the order of the quantum phase transitions. This highlights the strength of the combined NLCE+DMRG approach for detecting and analyzing complex ordered phases in light–matter coupled systems.

6. Frustration Phenomena on the Sawtooth Chain

In the following, we consider the Dicke-Ising model on the sawtooth chain. In contrast to the simple chain, it exhibits geometrical frustration for antiferromagnetic Ising interactions, meaning that not all bonds can be satisfied at the same time. First, we review known results for the transverse-field Ising model (TFIM) on this lattice and derive an effective low-field model for it. Then, we apply the self-consistent matter Hamiltonian of the Dicke-Ising model to the same geometry. The combined NLCE+DMRG method was used to study the system and a high-order series expansion was carried out in the strong-coupling limit.

For ferromagnetic Ising interactions the universal behavior remains unchanged compared to the simple chain, since frustration does not play a role in this case.

6.1. TFIM on the Sawtooth Chain

The transverse-field Ising model (TFIM) on the sawtooth chain is a well-known example of a frustrated quantum system. Because of the triangular geometry, not all antiferromagnetic Ising interactions can be satisfied at once. In the absence of a magnetic file, this results in an exponentially large number of degenerate ground states relative to the system size and in only short-range correlations at zero temperature [20].

Applying a transverse field introduces quantum fluctuations, which lifts the degeneracy and selects a unique ground state. Instead of giving rise to an ordered phase (as in the "order-by-disorder" mechanism), these fluctuations keep the system disordered. This is known as "disorder-by-disorder" [20, 21]. Even an infinitesimal small transverse field opens a gap and lifts the degeneracy. In the present case, this does not lead to order-by-disorder, but rather keeps the system in a disordered quantum phase without long-range magnetic order.

In the opposite case of strong fields, the system becomes a simple paramagnet. High-order series expansions show that there is no phase transition in between, the system remains disordered throughout [21].

6.1.1. Frustrated Ising Limit

To better understand the frustrated Ising limit ($h = 0$) of the TFIM (Equation 9) with antiferromagnetic Ising interactions, it is useful to derive an effective model by transitioning

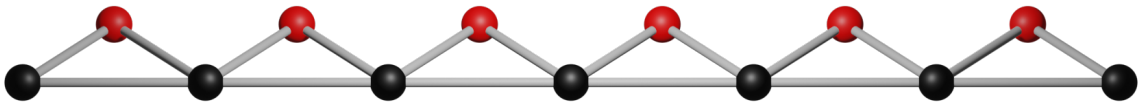

Figure 8: The sawtooth chain. The base spins in black and the apex spins in red.

to the dual picture of the lattice (Figure 9). In this representation, each bond of the sawtooth chain corresponds to a site of the dual lattice. By identifying the first-order processes of the model, one can construct an effective Hamiltonian.

We begin by noting that the ground state of the TFIM in the absence of a transverse field consists of one unsatisfied (ferromagnetic) bond per triangle. This leads to a ground-state energy density in this limit of

$$\frac{E_{0,\text{Ising}}}{N} = -\frac{|J|}{2} \tag{44}$$

with J the Ising coupling strength.

We now examine the effect of a single spin flip, introduced by the transverse field, on the ground-state manifold. Two cases must be distinguished: flipping an apex spin (red in Figure 8) or flipping a base spin (black in Figure 8). An apex spin flip affects two bonds, while a base spin flip affects four bonds. This gives rise to an effective Hamiltonian featuring both two-spin and four-spin interaction terms. Thus, the effective Hamiltonian in first-order degenerate perturbation theory in the degenerate ground-state space has the approximate form

$$\hat{\mathcal{H}}_{\text{eff}} \approx h \left[\sum_i \tau_i^x \tau_{i+2}^x + \sum_k \tau_k^x \tau_{k+1}^x \tau_{k+2}^x \tau_{k+3}^x \right] , \tag{45}$$

with pseudo-spins $\frac{1}{2}\,\tau$ defined on the dual lattice.

To determine the actual first-order contributions, it is necessary to ensure that the configuration remains within the ground-state manifold of the pure Ising model after a spin flip. This condition corresponds to maintaining the total number of frustrated bonds on the sawtooth chain. In the dual picture, this requirement translates to quasi-particle number conservation. We achieve this by rewriting the effective Hamiltonian in terms of raising and lowering operators,

$$\tau^{\pm} = \tau^x \pm \mathrm{i}\tau^y \quad \Rightarrow \quad \tau^x = \frac{\tau^+ + \tau^-}{2} , \tag{46}$$

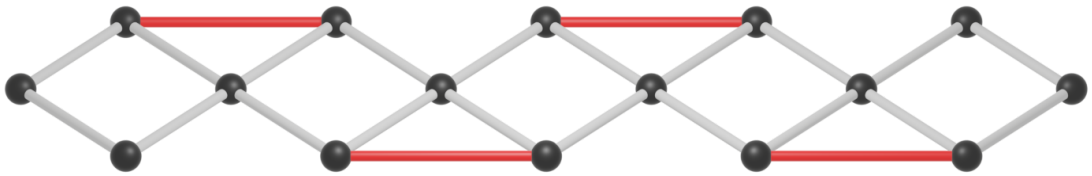

Figure 9: Visualization of the effective low-field model on the diamond chain. Four-spin interactions are represented as plaquettes (gray diamonds), and two-spin interactions are shown in red.

and retaining only the terms that contain an equal number of τ^+ and τ^- operators. The effective Hamiltonian for the TFIM in the Ising limit on the sawtooth chain, up to first order, then becomes

$$\begin{aligned}\hat{\mathcal{H}}_{\text{eff}} = \frac{h}{4}\Bigg[\sum_n \left(\tau^+_{3n}\tau^-_{3n+2} + \tau^-_{3n-2}\tau^+_{3n}\right) \\ + \frac{h}{16}\Bigg[\sum_n \left(\tau^+_{3n-2}\tau^+_{3n-1}\tau^-_{3n}\tau^-_{3n+1} + \tau^+_{3n-2}\tau^-_{3n-1}\tau^+_{3n}\tau^-_{3n+1}\right. \\ \left. + \tau^-_{3n-2}\tau^+_{3n-1}\tau^-_{3n}\tau^+_{3n+1} + \text{h.c.}\right)\Bigg].\end{aligned} \tag{47}$$

Now, in the dual model the Hamiltonian conserves the *total* number of quasiparticles, which corresponds to the total number of frustrated bonds in the original sawtooth chain. However, in addition to global conservation, we must also ensure that the *local* constraint, that each triangle contains exactly one frustrated bond, is respected. This condition is equivalent to having exactly one quasiparticle per diamond in Figure 9. The dual model is therefore constrained to a filling fraction $\nu = 1/3$.

In the ground-state manifold of the TFIM on the sawtooth chain, each triangle hosts one frustrated bond. A frustrated bond can either be located on the baseline or on one of the legs of the triangle. The simplest way to enforce this local rule in the dual model is by introducing appropriate projectors into the Hamiltonian Equation 47. These projectors ensure that only processes consistent with this constraint are allowed.

Let us first consider the two-spin interaction, which moves a frustrated bond from one leg

of a triangle to the other. This operation is only possible if the baseline of the triangle is *not* frustrated. Otherwise, flipping the apex spin would create frustrated bonds on both legs and leave the baseline frustrated, resulting in three frustrated bonds within a single triangle violating the one-per-triangle rule. Therefore, before carrying out the two-spin process, we must check in the dual model that the site corresponding to the baseline bond is unoccupied by a quasiparticle.

Next, we turn to the four-spin interaction. This process affects two triangles simultaneously, as it originates from flipping a baseline spin shared by both. Each baseline spin is connected to two bonds in the triangle on its left and two bonds in the triangle on its right. For the four-spin process to remain within the ground-state manifold, both the left and right triangle initially must contain the frustrated bond on a bond connected to the flipped baseline spin. This can be implemented by checking that, in the left triangle, the left leg is not frustrated, and in the right triangle, the right leg is not frustrated.

The projectors in the dual model are defined as

$$\hat{\mathcal{P}}_i \coloneqq (1 - \hat{n}_i)\,, \tag{48}$$

where the number operator $\hat{n}_i$ measures whether site i in the dual picture is occupied by a quasiparticle. If $\hat{n}_i = 0$, the projector equals one and leaves the Hamiltonian unchanged; if $\hat{n}_i = 1$, the projector vanishes and removes the corresponding term from the Hamiltonian. In terms of Pauli matrices, the number operator can be expressed as

$$\hat{n}_i = \frac{\tau_i^+ \tau_i^-}{4}\,. \tag{49}$$

The final effective Hamiltonian for the dual model, which conserves both the total and the local number of quasiparticles, reads

$$\begin{aligned}\hat{\mathcal{H}}_{\text{eff}} = \frac{h}{4}\Bigg[\sum_n \left(\tau_{3n}^+ \tau_{3n+2}^- + \tau_{3n+2}^- \tau_{3n}^+\right)\hat{\mathcal{P}}_{3n+1}\Bigg] \\ + \frac{h}{16}\Bigg[\sum_n \big(\tau_{3n-2}^+ \tau_{3n-1}^+ \tau_{3n}^- \tau_{3n+1}^- + \tau_{3n-2}^+ \tau_{3n-1}^- \tau_{3n}^- \tau_{3n+1}^+ \\ + \tau_{3n-2}^+ \tau_{3n-1}^- \tau_{3n}^+ \tau_{3n+1}^- + \text{h.c.}\big)\hat{\mathcal{P}}_{3n-3}\hat{\mathcal{P}}_{3n+2}\Bigg]\,.\end{aligned} \tag{50}$$

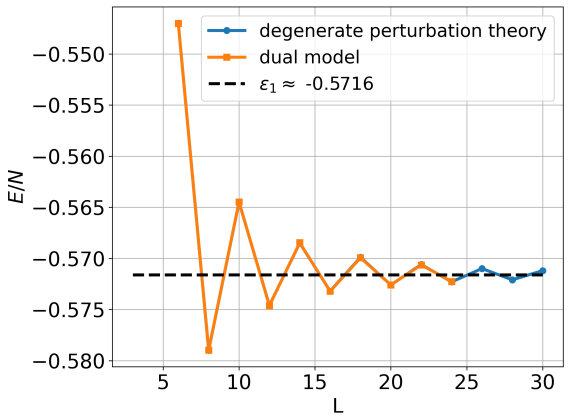

Figure 10: Ground-state energy of the dual model (orange) and first-order correction of the sawtooth chain (blue) from degenerate perturbation theory. Both approaches agree exactly, yielding an estimate for the first-order coefficient $\varepsilon_1 \approx -0.5716$.

This dual model can be benchmarked against the exact first-order degenerate perturbation theory for the sawtooth chain. The corresponding calculation is implemented in Python by enumerating all periodic configurations within the ground-state manifold (one frustrated bond per triangle) for system sizes of up to 30 sites. For each configuration, we determine which spin flips keep the system within the manifold. Allowed flips contribute to the first-order correction, whereas forbidden flips do not. This yields a matrix that can be diagonalized to obtain the smallest eigenvalue, corresponding to the first-order correction to the ground-state energy of the Ising model in a transverse field.

The dual model is solved via exact diagonalization (ED) with periodic boundary conditions, as described in subsection 3.2. Results were obtained for clusters of up to eight plaquettes (24 spins). As expected from first-order perturbation theory, the energy depends linearly on h. The constant term corresponds to the zeroth-order energy, i.e. the ground-state energy of the pure Ising model (Equation 44). Setting $h = 1$ reproduces exactly the first-order correction for the sawtooth chain.

The comparison of both approaches is shown in Figure 10 as a function of the system size L. For each L, the two methods yield identical results, as expected, since both compute the same physical quantity. The values converge to $\varepsilon_1 \approx -0.5716$.

In summary, the dual model provides a clear framework for analyzing the first-order processes of the TFIM on the sawtooth chain in the frustrated Ising limit. Its predictions agree exactly with first-order degenerate perturbation theory confirming the validity of the construction.

6.2. Dicke-Ising model on the sawtooth chain

The Dicke-Ising model can be again described by the effective matter Hamiltonian Equation 27, which is a TFIM with a self-consistent transverse field plus an extra longitudinal field. We can use the same methods as for the 1D chain because the sawtooth chain is a quasi-1D lattice geometry, which still has an entanglement low enough to perform DMRG. The NLCE formula Equation 34 has to be adjusted to a two-site-unit-cell as for the antiferromagnetic linear chain to

$$e_0^{(N)} = E_0(C_N) - E_0(C_{N-2})\,. \tag{51}$$

For the sawtooth chain one can do a cluster expansion in unit cells (even N) and one in triangles (odd N), where N is the cluster size. In contrast to the antiferromagnetic linear chain, no additional environmental field is required here, since the choice of unit cell in the sawtooth geometry already fixes the orientation consistently. In the following, besides the phase diagram for the sawtooth chain, the covergence between the two expansion is analyzed, too.

6.2.1. Results

One of the most interesting features of the TFIM on the frustrated sawtooth chain is the disorder-by-disorder mechanism. In this scenario, quantum fluctuations induced by a transverse field stabilize a disordered ground state rather than selecting an ordered one. The question arises whether this mechanism, which is well established in the pure TFIM, also manifests itself in the Dicke–Ising system, where the spins interact collectively with a bosonic mode. In this case the leading nontrivial contributions arise only in second order of perturbation theory, as effective spin–photon processes necessarily involve two interaction vertices. In particular, the interplay between frustration, spin–photon coupling, and longitudinal fields promises a richer phase structure. In the following, we first focus on the case without a longitudinal field and subsequently discuss the modifications that occur once a finite longitudinal field is introduced.

Case without longitudinal field. The results for vanishing longitudinal field are shown in Figure 11. The ground-state energy displays a smooth and continuous dependence on the spin–photon coupling strength g, with no indication of a singularity or kink that would signal a quantum phase transition. This observation is already a strong hint that the system avoids

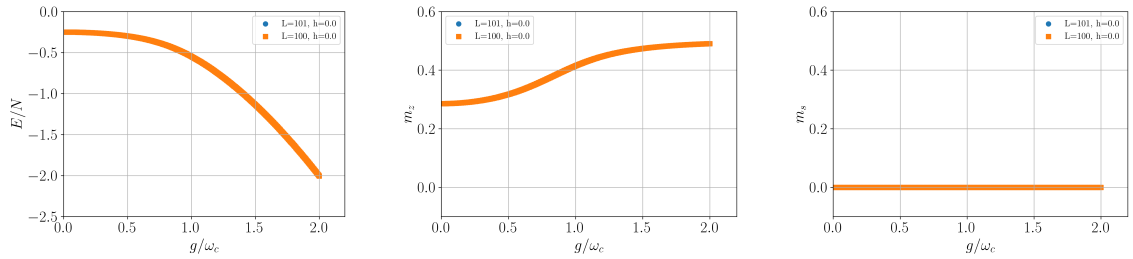

Ground-state energy density Magnetization Staggered magnetization

Figure 11: DMRG results for a NLCE with $N = 100$ and $N = 101$ for $J = 0.5$ and $h = 0.0$. The disorder-by-disorder effect is clearly visible.

conventional symmetry breaking. At the same time, the transversal magnetization remains finite throughout the full parameter range. Physically, this means that the Dicke–Ising system is driven into the superradiant phase by an infinitesimal perturbation of the light–matter coupling, i.e., there exists no finite critical threshold. This behavior is in perfect agreement with the disorder-by-disorder mechanism: frustration prevents the formation of long-range magnetic order, while the coupling to the bosonic mode immediately favors a collective superradiant state.

The staggered magnetization on the baseline of the sawtooth chain, plotted in the third panel, is identically zero within numerical accuracy. Consequently, no antiferromagnetic order arises in the system. Taken together with the finite transversal magnetization, this result confirms that the ground state is paramagnetic with respect to spin correlations, yet superradiant due to the photon field. Thus, the Dicke-Ising system at $h = 0$ reproduces the essential physics of the TFIM: quantum fluctuations stabilize a disordered, paramagnetic ground state which is, however, immediately destabilized by infinitesimal coupling to the bosonic field, entering the superradiant regime.

Case with finite longitudinal field. The situation changes qualitatively when a longitudinal field is applied. In this case, the degeneracy of the frustrated manifold is lifted already at the classical level ($h = 0$), such that a magnetically ordered phase becomes energetically favorable at small values of the coupling g. Our DMRG results, shown in Figure 13, indeed reveal that the system initially resides in a magnetically ordered state with zero photon density rather than directly entering the superradiant phase. Only upon further increasing the coupling the system undergoes a quantum phase transition into the paramagnetic superradiant phase.

The character of this transition is markedly different from the continuous crossover observed at $h = 0$. The ground-state energy exhibits a distinct non-analyticity, with a visible kink that is absent in the case of zero longitudinal field. Simultaneously, the order parameters, i.e., the magnetization and the staggered magnetization, show finite jumps at the phase transition. This clear discontinuity in the thermodynamic observables is the evidence of a first-order quantum phase transition. Physically, the system switches abruptly between two competing ordered states: a magnetically ordered phase stabilized by the longitudinal field and a paramagnetic superradiant phase favored by the light–matter interaction.

Comparison of NLCE expansions. An important technical aspect concerns the convergence properties of cluster expansions used in our DMRG simulations. We compared two different cluster constructions, namely the unit-cell expansion with $N = 100$ sites (Figure 12) and the triangular expansion with $N = 101$ sites (Figure 13). The results indicate that the triangular expansion converges significantly better, especially in the regime of intermediate coupling. While the unit-cell expansion shows unphysical artifacts, such as oscillations in the order parameters, the triangular expansion produces stable and physically consistent results. This difference can be understood from symmetry considerations. The triangular expansion respects the geometric symmetries of the sawtooth chain better, thereby capturing the essential physics of frustration and collective coupling more accurately.

Summary. In summary, the Dicke–Ising model on the sawtooth chain exhibits two qualitatively distinct regimes. Without a longitudinal field, the disorder-by-disorder mechanism persists: the system avoids magnetic ordering and enters the superradiant phase immediately at infinitesimal coupling strength. With a finite longitudinal field, by contrast, a magnetically ordered state becomes stabilized at small coupling, and the transition into the superradiant phase is shifted to finite g, occurring as a sharp first-order transition. These findings highlight the delicate interplay between frustration, spin–boson coupling, and longitudinal fields, and they emphasize the necessity of carefully chosen NLCE expansions to obtain reliable numerical results.

6.2.2. Series expansion in the strong coupling limit

It is also possible to study the sawtooth chain in the strong coupling limit using a series-expansion approach, as outlined in subsection 3.4. For the effective Hamiltonian Equation 27,

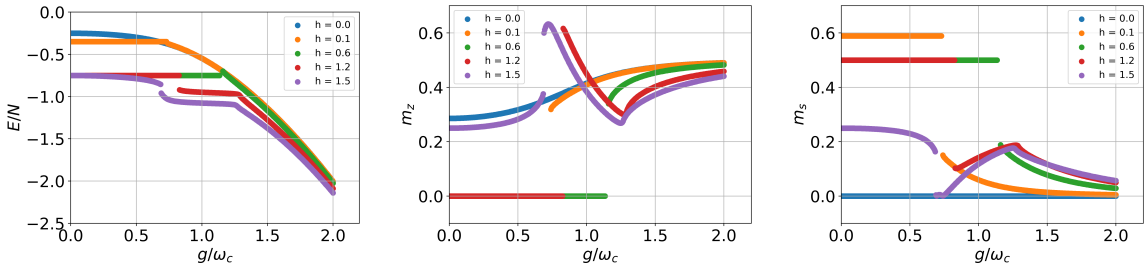

Ground-state energy Magnetization Staggered magnetization

Figure 12: DMRG results for a NLCE with $N = 100$ and $J = 0.5$ based on unit cell expansion.

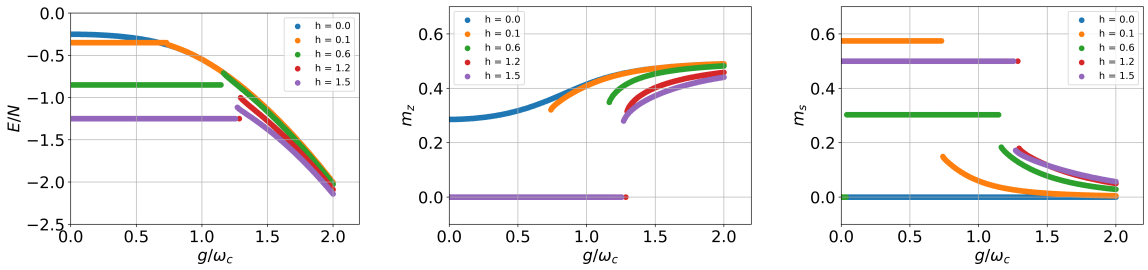

Ground-state energy Magnetization Staggered magnetization

Figure 13: DMRG results for a NLCE with $N = 101$ and $J = 0.5$ based on triangular expansion.

we choose the transverse field as the unperturbed part and treat the Ising coupling together with the longitudinal field as perturbations:

$$\hat{\mathcal{H}}_0 = -2m_z \sum_i \sigma_i^z, \tag{52}$$

$$V = J \sum_{\langle i,j \rangle} \sigma_i^x \sigma_j^x + h \sum_i \sigma_i^x. \tag{53}$$

The unperturbed Hamiltonian $\hat{\mathcal{H}}_0$ has a unique ground state,

$$|0\rangle = |\uparrow \cdots \uparrow\rangle \equiv |\Uparrow\rangle ,$$

with eigenvalue $E_0^0 = -2m_z N$. Within the framework of Löwdin's projection operator formalism [60], the relevant objects are

$$\begin{aligned} P &= 1 - Q = |0\rangle \langle 0| , \quad \text{projector onto the ground state,} \\ V &= J \sum_{\langle i,j \rangle} \sigma_i^x \sigma_j^x + h \sum_i \sigma_i^x, \quad \text{perturbation,} \\ S &= Q \frac{1}{E_0^0 - \hat{\mathcal{H}}_0} Q, \quad \text{resolvent.} \end{aligned} \tag{54}$$

A difficulty arises because the expansion depends explicitly on the magnetization m_z, which itself must be determined self-consistently. To resolve this, we employ the Hellmann–Feynman theorem [61], which relates the derivative of the ground-state energy with respect to a parameter to the expectation value of the derivative of the Hamiltonian with respect to that parameter. For the present case this yields

$$m_z = -\frac{1}{4} \frac{\mathrm{d}}{\mathrm{d}m_z} \left(\frac{E_0}{N} \right) . \tag{55}$$

In practice, one first expands the ground-state energy in powers of J and h, then takes the derivative to obtain a series for m_z that still depends on m_z itself. Solving this relation order by order provides a consistent expansion of the magnetization as a function of J and h. Substituting the result back into the energy series subsequently yields a fully self-consistent expansion for the ground-state energy.

The series was computed up to the 13th order for clusters of size 26 and 24. In order to

approach the thermodynamic limit, a linked-cluster expansion was employed, where the contributions of the 24-site cluster were systematically subtracted from those of the 26-site cluster. This procedure effectively eliminates finite-size effects and allows for a controlled extrapolation. The resulting expansions of the ground-state energy and the magnetization are displayed in Figure 14 for three representative values of J/h. In addition, DMRG+NLCE results are plotted on top of the series to verify and confirm their convergence.

For $J = 0$, the model reduces to the Dicke model, which is lattice-independent. As shown in Figure 14, a clear second-order quantum phase transition occurs at $h = 1$, in full agreement with expectations. The critical behavior in the magnetization at this transition point is made visible by a Dlog-Padé analysis. The DMRG data is found to be in excellent agreement with the series expansion, thereby validating the approach.

For $J/h = 11/10$, the Padé extrapolation follows the DMRG results significantly longer than the bare series, as anticipated. In this regime, the DMRG reveals a first-order quantum phase transition. Beyond this point, the series expansion ceases to be applicable, which is consistent with the breakdown expected in the presence of discontinuous behavior.

Finally, for $h = 0$, the model reduces to the quantum transverse-field Ising model (QTFIM) on the sawtooth chain. Within the investigated parameter range, no phase transition was observed. Once again, the Padé approximants capture the DMRG results over a broader range than the bare series, highlighting their effectiveness in extending the convergence of the expansion.

In summary, the high-order series expansion provides a reliable description of the ground-state properties across different parameter regimes. The combination with Padé extrapolations significantly extends the radius of convergence, and the excellent agreement with DMRG+NLCE benchmarks demonstrates the robustness and accuracy of the approach.

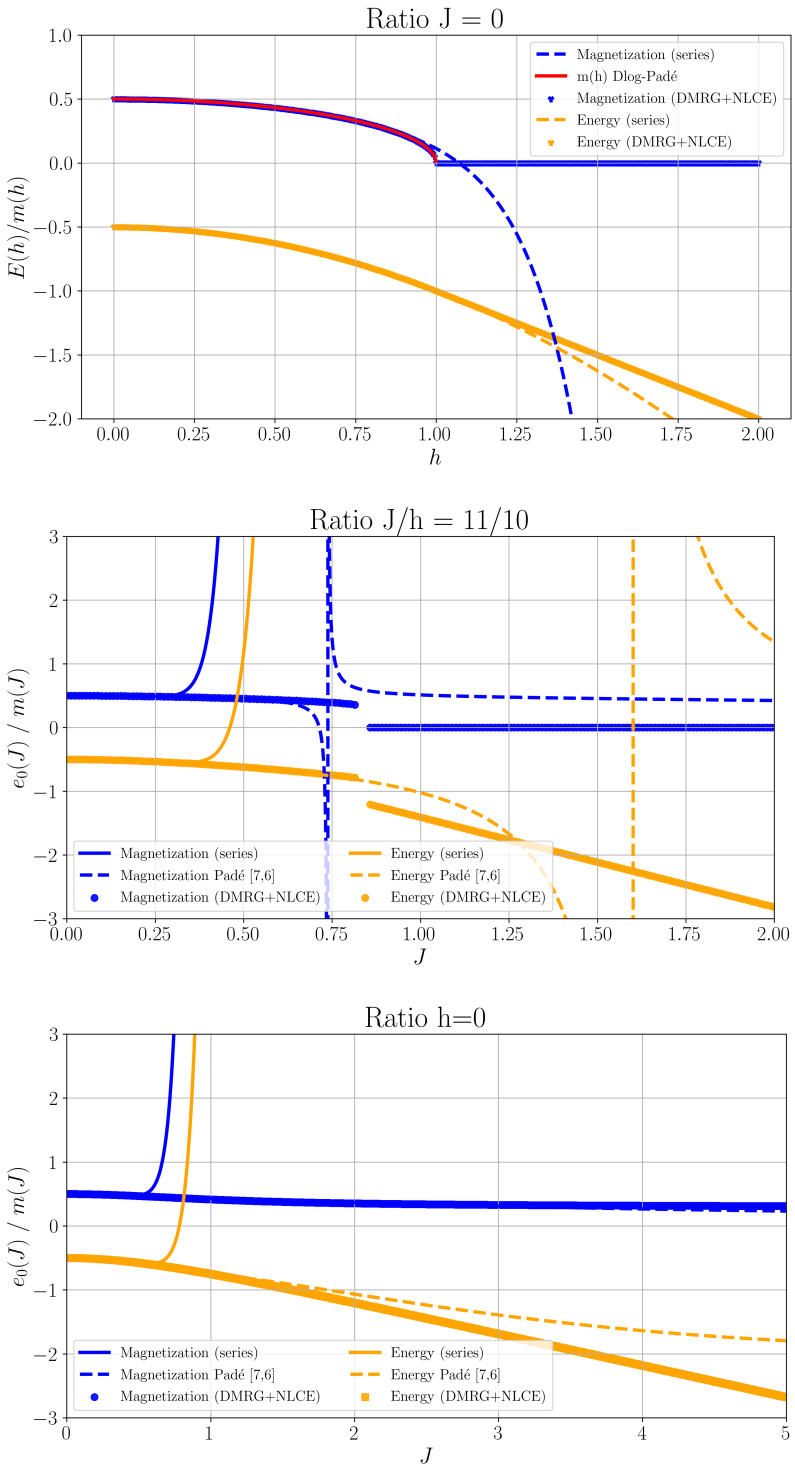

Figure 14: Series expansion with Padé approximants in the strong-coupling limit of the sawtooth chain, compared with DMRG+NLCE results.

7. Conclusion

In this thesis we investigated the ground-state properties of the Dicke-Ising model on the one-dimensional chain and on the frustrated sawtooth chain by using an effective self-consistent matter Hamiltonian [15]. To analyze this system, we combined the numerical linked-cluster expansion (NLCE) with high-precision density-matrix renormalization group (DMRG) simulations and supplemented the study with perturbative series expansions.

For the ferromagnetic chain, we established a reliable criterion to distinguish between first- and second-order quantum phase transitions by comparing the self-consistent ground-state energies with mean-field predictions. This allowed us to determine the multicritical point at $\varepsilon/\omega_c \approx 0.200124$ with high precision, in excellent agreement with previous quantum Monte Carlo estimates [18]. Our results confirm the change of transition order as a function of model parameters and demonstrate the accuracy of the NLCE+DMRG approach for locating such features.

In the case of antiferromagnetic couplings on the chain, we identified the antiferromagnetic superradiant phase, characterized by the coexistence of antiferromagnetic order in the matter sector and superradiant order in the photon field. We precisely located the phase boundaries and determined the transition orders: a continuous transition between the antiferromagnetic normal and antiferromagnetic superradiant phases, and a clear first-order transition between the antiferromagnetic superrradiant and paramagnetic superradiant regimes. These results highlight the ability of our method to resolve complex competing orders in coupled spin-boson systems.

Turning to the sawtooth chain, we first revisited the transverse-field Ising model and constructed an effective low-field dual Hamiltonian. Exact diagonalization confirmed the validity of this dual description by reproducing the first-order correction to the Ising ground-state energy. Applying the Dicke-Ising framework to the sawtooth geometry, we found that the well-known disorder-by-disorder mechanism persists: without a longitudinal field, the system avoids magnetic ordering and enters the superradiant phase immediately at infinitesimal coupling. In contrast, with a finite longitudinal field, the degeneracy of the frustrated manifold is lifted, leading to a magnetically ordered phase at small couplings and a sharp first-order transition into the superradiant phase at larger couplings. Furthermore, we showed that the triangular cluster expansion within NLCE provides superior convergence compared to the unit-cell expansion, underlining the importance of symmetry-adapted cluster choices for frustrated systems. Finally, a high-order series expansion in the strong-coupling regime

confirmed the absence of additional phase transitions and complemented the numerical analysis.

Overall, the results of this thesis demonstrate how the interplay of frustration, collective spin-photon coupling, and external fields gives rise to rich and unconventional quantum phases. The combined NLCE+DMRG approach proved to be a powerful tool to characterize phase boundaries and transition orders in light-matter coupled systems.

8. Outlook

In the future, it would be interesting to investigate the Dicke-Ising model on other lattice geometries. For example, the square lattice could provide further insights into the stability of the intermediate antiferromagnetic superradiant phase, while the triangular lattice offers the opportunity to explore whether the order-by-disorder mechanism [20, 21] is realized in analogy to the disorder-by-disorder scenario observed on the sawtooth chain. More generally, extensions to other two- or even three-dimensional lattices would be highly desirable. However, this requires improved numerical methods, since the single clusters needed for the NLCE can no longer be solved efficiently with DMRG due to the rapid growth of entanglement in two dimensions. A natural way forward would be to employ projected entangled-pair states (PEPS) [62] or directly work with infinite PEPS (iPEPS) [63], which provide a powerful tensor network framework to access the thermodynamic limit in two dimensions without the need for a cluster expansion.

Another promising direction is to incorporate long-range spin–spin interactions, either cavity-mediated or intrinsic dipolar couplings, into static light-matter models. Many experimental platforms naturally feature interactions extending beyond nearest neighbors, such as Rydberg-dressed atoms or magnetic dipoles. Including such long-range interactions alongside the cavity field can lead to much richer phase behavior. Recent work on the long-range Dicke-Ising model demonstrates the melting of devil's staircases and the emergence of a plethora of intermediate phases that break translational symmetry and carry finite photon density [64]. Long-range couplings can stabilize complex multi-sublattice superradiant orders, which do not appear in short-range models. Systematically studying how the range and profile of interactions affect the ground-state phase diagram would clarify the competition between local magnetic order and global cavity-mediated coupling.

Another interesting extension is to consider setups with multiple photonic modes. While a

single cavity mode effectively induces a uniform infinite-range interaction between all spins, additional modes with different spatial profiles can generate tunable, even sign-changing and quasi-local interactions; this has been shown theoretically and experimentally in multimode cavity QED [65–67]. Circuit-QED platforms further provide flexible resonator networks to realize engineered photon-mediated couplings [68]. Studying how competing cavity modes affect the stability and nature of superradiant phases could reveal novel ordered states, for example situations with multiple independent superradiant order parameters or glassy behavior arising from frustrated light-mediated couplings.

In parallel, it would also be valuable to study other spin Hamiltonians beyond the Ising case. For instance, XY or Heisenberg interactions may give rise to qualitatively different ground states when combined with collective spin-photon coupling. Such models could host superradiant-like transitions or hybrid phases where magnetic order and photon condensation coexist. Exploring these scenarios would provide a broader understanding of how different types of spin correlations influence light–matter coupled systems.

Beyond lattice geometries, it would also be highly interesting to study the effect of light-matter coupling on topological phases of matter. A prominent example is Kitaev's toric code [69], where it is an open question whether the topological order remains robust in the presence of a light perturbation or whether it immediately breaks down. Understanding the interplay between topological order and collective spin–photon coupling would open a new avenue for research, potentially connecting the fields of quantum optics, frustrated magnetism, and topological quantum matter.

A. DMRG Parameters

All DMRG calculations were performed using the `ITensor.jl` package. The DMRG simulations were carried out with up to 200 sweeps and an increasing schedule of maximum bond dimensions $\texttt{maxdim} = [10, 20, 50, 100, 150, 200, 250, 300]$. This allowed for an efficient initial approximation with small bond dimensions, followed by a refinement of the accuracy in later sweeps. A very strict truncation tolerance of $\texttt{tol} = 10^{-10}$ was imposed, such that the discarded weight remained negligible throughout. The employed `DMRGObserver` monitored both local observables (S^z) and the convergence of the energy, with the same tolerance used as stopping criterion. In this way, the ground states were obtained with essentially machine precision.

Within the NLCE approach, DMRG was performed for each cluster while solving a self-consistency condition: the calculated order parameter had to match the initially assumed value. This self-consistency loop was iterated to the same tolerance of 10^{-10}, ensuring compatibility with the DMRG accuracy.

To traverse the phase diagram, we employed an adiabatic continuation scheme. The converged ground state from the previous parameter point was used as the initial wavefunction ψ_0, and likewise the previously determined order parameter served as the initial guess for the next self-consistency step. This procedure significantly accelerated the convergence of the self-consistency loop and allowed for an efficient exploration of the parameter space.

B. Exact the solution of the quantized transverse field Ising model for the chain geometry

The quantized transverse field Ising model [15] is the Dicke-Ising model with no longitudinal field. The effective matter Hamiltonian Equation 27 for the Dicke-Ising model simplifies to a transverse field Ising model with a self-consistent transverse field. The Hamiltonian is

$$\hat{\mathcal{H}}\left(m_z\right) = -2m_z \sum_i \sigma_i^z + J \sum_{\langle i,j \rangle} \sigma_i^x \sigma_j^x \,. \tag{56}$$

For the TFIM on the chain an exact solution is given by Pfeuty [34]. The magnetization is

$$\begin{aligned} m =& \frac{1}{2}(L(0) + \lambda L(1)), \quad \lambda = \frac{J}{4m_z} \\ L(n) =& \frac{1}{\pi} \int_0^\pi \mathrm{d}k \Lambda_k^{-1} \cos(kn) \\ \Lambda_k^2 =& 1 + \lambda^2 + 2\lambda \cos(k) \end{aligned} \tag{57}$$

and the ground-state energy per site is

$$\frac{E_0}{N} = \frac{1}{\pi} \int_0^\pi \mathrm{d}k \Lambda_k + g^2 m^2 \,. \tag{58}$$

Now it is possible to calculate the first-order transition because the energy of the magnetically ordered normal phase is exactly $-J$. The critical value of the transition then is the intersection of this energy with the energy of the TFIM Equation 58. This gives

$$g_c = 1.8292988956 \cdot \sqrt{J} \,. \tag{59}$$

References

[1] P. Kirton, M. M. Roses, J. Keeling, and E. G. Dalla Torre, "Introduction to the dicke model: From equilibrium to nonequilibrium, and vice versa", *Advanced Quantum Technologies*, vol. 2, no. 1–2, Oct. 2018, ISSN: 2511-9044. DOI: 10.1002/qute.201800043. [Online]. Available: http://dx.doi.org/10.1002/qute.201800043.

[2] A. Frisk Kockum, A. Miranowicz, S. De Liberato, S. Savasta, and F. Nori, "Ultrastrong coupling between light and matter", *Nature Reviews Physics*, vol. 1, no. 1, 19–40, Jan. 2019, ISSN: 2522-5820. DOI: 10.1038/s42254-018-0006-2. [Online]. Available: http://dx.doi.org/10.1038/s42254-018-0006-2.

[3] R. H. Dicke, "Coherence in spontaneous radiation processes", *Phys. Rev.*, vol. 93, no. 1, pp. 99–110, 1954. DOI: 10.1103/PhysRev.93.99.

[4] K. Hepp and E. H. Lieb, "On the superradiant phase transition for molecules in a quantized radiation field: The dicke maser model", *Annals of Physics*, vol. 76, no. 2, pp. 360–404, 1973. DOI: 10.1016/0003-4916(73)90039-0.

[5] Y. K. Wang and F. T. Hioe, "Phase transition in the dicke model of superradiance", *Phys. Rev. A*, vol. 7, no. 3, pp. 831–836, 1973. DOI: 10.1103/PhysRevA.7.831.

[6] K. Rzażewski, K. Wódkiewicz, and W. Żakowicz, "Phase transitions, two-level atoms, and the A^2 term", *Physical Review Letters*, vol. 35, no. 7, pp. 432–434, 1975. DOI: 10.1103/PhysRevLett.35.432.

[7] P. Nataf and C. Ciuti, "No-go theorem for superradiant quantum phase transitions in cavity qed and counter-example in circuit qed", *Nature Communications*, vol. 1, p. 72, 2010. DOI: 10.1038/ncomms1069.

[8] O. Viehmann, J. von Delft, and F. Marquardt, "Superradiant phase transitions and the standard description of circuit qed", *Physical Review Letters*, vol. 107, no. 11, p. 113 602, 2011. DOI: 10.1103/PhysRevLett.107.113602.

[9] T. Niemczyk *et al.*, "Circuit quantum electrodynamics in the ultrastrong-coupling regime", *Nature Physics*, vol. 6, pp. 772–776, 2010. DOI: 10.1038/nphys1730.

[10] C. Weisbuch, M. Nishioka, A. Ishikawa, and Y. Arakawa, "Observation of the coupled exciton-photon mode splitting in a semiconductor quantum microcavity", *Phys. Rev. Lett.*, vol. 69, pp. 3314–3317, 1992. DOI: 10.1103/PhysRevLett.69.3314.

[11] H. Deng, H. Haug, and Y. Yamamoto, "Exciton-polariton bose-einstein condensation", *Rev. Mod. Phys.*, vol. 82, no. 2, pp. 1489–1537, 2010. DOI: 10.1103/RevModPhys.82.1489.

[12] K. Nagarajan, A. Thomas, and T. W. Ebbesen, "Chemistry under vibrational strong coupling", *ACS Photonics*, vol. 5, no. 1, pp. 203–210, 2018. DOI: 10.1021/acsphotonics.7b00680.

[13] J. Bloch, A. Cavalleri, V. Galitski, M. Hafezi, and A. Rubio, "Strongly coupling to the vacuum field", *Science*, vol. 373, no. 6551, eabd0336, 2021. DOI: 10.1126/science.abd0336.

[14] Y. Zhang, L. Yu, J. Q. Liang, G. Chen, S. Jia, and F. Nori, "Quantum phases in circuit qed with a superconducting qubit array", *Scientific Reports*, vol. 4, no. 1, p. 4083, 2014, ISSN: 2045-2322. DOI: 10.1038/srep04083. [Online]. Available: https://doi.org/10.1038/srep04083.

[15] J. Rohn, M. Hörmann, C. Genes, and K. P. Schmidt, "Ising model in a light-induced quantized transverse field", *Phys. Rev. Res.*, vol. 2, p. 023 131, 2 May 2020. DOI: 10.1103/PhysRevResearch.2.023131. [Online]. Available: https://link.aps.org/doi/10.1103/PhysRevResearch.2.023131.

[16] E. Cortese, L. Garziano, and S. De Liberato, "Polariton spectrum of the dicke-ising model", *Phys. Rev. A*, vol. 96, no. 5, p. 053 861, 2017. DOI: 10.1103/PhysRevA.96.053861.

[17] A. Schellenberger and K. P. Schmidt, "(almost) everything is a dicke model - mapping non-superradiant correlated light-matter systems to the exactly solvable dicke model", *SciPost Physics Core*, vol. 7, no. 3, Jul. 2024, ISSN: 2666-9366. DOI: 10.21468/scipostphyscore.7.3.038. [Online]. Available: http://dx.doi.org/10.21468/SciPostPhysCore.7.3.038.

[18] A. Langheld, M. Hörmann, and K. P. Schmidt, *Quantum phase diagrams of dicke-ising models by a wormhole algorithm*, 2024. arXiv: 2409.15082 [cond-mat.str-el]. [Online]. Available: https://arxiv.org/abs/2409.15082.

[19] J. A. Koziol, A. Langheld, and K. P. Schmidt, "Melting of devil's staircases in the long-range dicke-ising model", *Physical Review B*, vol. 111, no. 22, p. 224 427, 2025.

[20] R. Moessner and S. L. Sondhi, "Ising models of quantum frustration", *Physical Review B*, vol. 63, no. 22, p. 224 401, 2001. DOI: 10.1103/PhysRevB.63.224401.

[21] D. J. Priour, M. P. Gelfand, and S. L. Sondhi, "Disorder from disorder in a strongly frustrated transverse-field ising chain", *Phys. Rev. B*, vol. 64, p. 134 424, 13 Sep. 2001. DOI: 10.1103/PhysRevB.64.134424.

[22] Anonymous, "Proceedings of the american physical society", *Phys. Rev.*, vol. 69, pp. 674–674, 11-12 Jun. 1946. DOI: 10.1103/PhysRev.69.674. [Online]. Available: https://link.aps.org/doi/10.1103/PhysRev.69.674.

[23] J. M. Raimond, M. Brune, and S. Haroche, "Collective strong coupling of rydberg atoms and a cavity field", *Phys. Rev. Lett.*, vol. 51, p. 1175, 1983. DOI: 10.1103/PhysRevLett.51.1175.

[24] R. J. Thompson, G. Rempe, and H. J. Kimble, "Observation of normal-mode splitting for an atom in an optical cavity", *Phys. Rev. Lett.*, vol. 68, pp. 1132–1135, 1992. DOI: 10.1103/PhysRevLett.68.1132.

[25] J. M. Raimond, M. Brune, and S. Haroche, "Manipulating quantum entanglement with atoms and photons in a cavity", *Rev. Mod. Phys.*, vol. 73, pp. 565–582, 2001. DOI: 10.1103/RevModPhys.73.565.

[26] G. Günter *et al.*, "Sub-cycle switch-on of ultrastrong light–matter interaction", *Nature*, vol. 458, pp. 178–181, 2009. DOI: 10.1038/nature07838.

[27] G. Rempe, H. Walther, and N. Klein, "Observation of quantum collapse and revival in a one-atom maser", *Physical review letters*, vol. 58, no. 4, p. 353, 1987.

[28] F. Todisco *et al.*, "Ultrastrong plasmon–exciton coupling by dynamic molecular aggregation", *ACS Photonics*, vol. 5, no. 1, pp. 143–150, 2018. DOI: 10.1021/acsphotonics.7b00554.

[29] F. Benz *et al.*, "Single-molecule optomechanics in "picocavities"", *Science*, vol. 354, no. 6313, pp. 726–729, 2016. DOI: 10.1126/science.aah5243. [Online]. Available: https://www.science.org/doi/abs/10.1126/science.aah5243.

[30] J. George *et al.*, "Multiple rabi splittings under ultrastrong vibrational coupling", *Phys. Rev. Lett.*, vol. 117, p. 153 601, 15 Oct. 2016. DOI: 10.1103/PhysRevLett.117.153601. [Online]. Available: https://link.aps.org/doi/10.1103/PhysRevLett.117.153601.

[31] M. Tavis and F. W. Cummings, "Exact solution for an n-molecule—radiation-field hamiltonian", *Phys. Rev.*, vol. 170, no. 2, pp. 379–384, 1968. DOI: 10.1103/PhysRev.170.379.

[32] E. Ising, "Beitrag zur theorie des ferromagnetismus", *Zeitschrift für Physik*, vol. 31, no. 1, pp. 253–258, 1925. DOI: 10.1007/BF02980577.

[33] L. Onsager, "Crystal statistics. i. a two-dimensional model with an order-disorder transition", *Phys. Rev.*, vol. 65, no. 3–4, pp. 117–149, 1944. DOI: 10.1103/PhysRev.65.117.

[34] P. Pfeuty, "The one-dimensional ising model with a transverse field", *Annals of Physics*, vol. 57, no. 1, pp. 79–90, 1970. DOI: 10.1016/0003-4916(70)90270-8.

[35] L. Zdeborová and F. Krzakala, "Statistical physics of inference: Thresholds and algorithms", *Advances in Physics*, vol. 65, no. 5, 453–552, Aug. 2016, ISSN: 1460-6976. DOI: 10.1080/00018732.2016.1211393. [Online]. Available: http://dx.doi.org/10.1080/00018732.2016.1211393.

[36] N. I. Alonso, C. You, *et al.*, "The mathematics of the ising model and neural networks", *Can, The Mathematics of the Ising Model and Neural Networks (January 01, 2025)*, 2025.

[37] T. Broderick, M. Dudik, G. Tkacik, R. E. Schapire, and W. Bialek, *Faster solutions of the inverse pairwise ising problem*, 2007. arXiv: 0712.2437 [q-bio.QM]. [Online]. Available: https://arxiv.org/abs/0712.2437.

[38] Y. Roudi, J. Tyrcha, and J. A. Hertz, "Ising model for neural data: Model quality and approximate methods for extracting functional connectivity", *Physical Review E*, vol. 79, no. 5, p. 051 915, 2009. DOI: 10.1103/PhysRevE.79.051915.

[39] T. O. Puel and T. Macrì, "Confined meson excitations in rydberg-atom arrays coupled to a cavity field", *Phys. Rev. Lett.*, vol. 133, p. 106 901, 10 Sep. 2024. DOI: 10.1103/PhysRevLett.133.106901. [Online]. Available: https://link.aps.org/doi/10.1103/PhysRevLett.133.106901.

[40] X.-F. Zhang, Q. Sun, Y.-C. Wen, W.-M. Liu, S. Eggert, and A.-C. Ji, "Rydberg polaritons in a cavity: A superradiant solid", *Phys. Rev. Lett.*, vol. 110, p. 090 402, 9 Feb. 2013. DOI: 10.1103/PhysRevLett.110.090402. [Online]. Available: https://link.aps.org/doi/10.1103/PhysRevLett.110.090402.

[41] A. Langheld, M. Hörmann, and K. P. Schmidt, *Raw data to "quantum phase diagrams of dicke-ising models by a wormhole algorithm"*, 2025. DOI: 10.5281/zenodo.15774230. [Online]. Available: https://doi.org/10.5281/zenodo.15774230.

[42] I. Brankov, V. A. Zagrebnov, and I. Tonchev, "Asymptotically exact solution of the generalized dicke model", *Theoretical and Mathematical Physics*, vol. 22, no. 1, pp. 13–20, 1975.

[43] R. Gibberd, "Equivalence of the dicke maser model and the ising model at equilibrium", *Australian Journal of Physics*, vol. 27, no. 2, pp. 241–248, 1974.

[44] J Vidal and S Dusuel, "Finite-size scaling exponents in the dicke model", *Europhysics Letters (EPL)*, vol. 74, no. 5, 817–822, Jun. 2006, ISSN: 1286-4854. DOI: 10.1209/epl/i2006-10041-9. [Online]. Available: http://dx.doi.org/10.1209/epl/i2006-10041-9.

[45] J. Reslen, L. Quiroga, and N. F. Johnson, "Direct equivalence between quantum phase transition phenomena in radiation-matter and magnetic systems: Scaling of entanglement", *Europhysics letters*, vol. 69, no. 1, p. 8, 2004.

[46] G. Liberti and R. L. Zaffino, "Thermodynamic properties of the dicke model in the strong-coupling regime", *The European Physical Journal B-Condensed Matter and Complex Systems*, vol. 44, no. 4, pp. 535–541, 2005.

[47] M. Rigol, T. Bryant, and R. R. P. Singh, "Numerical linked-cluster algorithms. i. spin systems on square, triangular, and kagomé lattices", *Phys. Rev. E*, vol. 75, p. 061 118, 6 Jun. 2007. DOI: 10.1103/PhysRevE.75.061118. [Online]. Available: https://link.aps.org/doi/10.1103/PhysRevE.75.061118.

[48] A. W. Sandvik, A. Avella, and F. Mancini, "Computational studies of quantum spin systems", in *AIP Conference Proceedings*, AIP, 2010. DOI: 10.1063/1.3518900. [Online]. Available: http://dx.doi.org/10.1063/1.3518900.

[49] A. M. Läuchli, "Numerical simulations of frustrated systems", in *Introduction to Frustrated Magnetism*, Springer Berlin Heidelberg, 2011, pp. 481–511.

[50] P. Weinberg and M. Bukov, "QuSpin: a Python package for dynamics and exact diagonalisation of quantum many body systems part I: spin chains", *SciPost Phys.*, vol. 2, p. 003, 2017. DOI: 10.21468/SciPostPhys.2.1.003. [Online]. Available: https://scipost.org/10.21468/SciPostPhys.2.1.003.

[51] P. Weinberg and M. Bukov, "QuSpin: a Python package for dynamics and exact diagonalisation of quantum many body systems. Part II: bosons, fermions and higher spins", *SciPost Phys.*, vol. 7, p. 020, 2019. DOI: 10.21468/SciPostPhys.7.2.020. [Online]. Available: https://scipost.org/10.21468/SciPostPhys.7.2.020.

[52] S. R. White, "Density matrix formulation for quantum renormalization groups", *Physical Review Letters*, vol. 69, pp. 2863–2866, 1992. DOI: 10.1103/PhysRevLett.69.2863.

[53] U. Schollwöck, "The density-matrix renormalization group in the age of matrix product states", *Annals of Physics*, vol. 326, pp. 96–192, 2011. DOI: 10.1016/j.aop.2010.09.012.

[54] M. Fishman, S. R. White, and E. M. Stoudenmire, "The ITensor software library for tensor network calculations", *SciPost Physics Codebases*, 2022. DOI: 10.21468/SciPostPhysCodeb.4.

[55] R. R. P. Singh, M. P. Gelfand, and D. A. Huse, "Ground states of low-dimensional quantum antiferromagnets", *Phys. Rev. Lett.*, vol. 61, pp. 2484–2487, 21 Nov. 1988. DOI: 10.1103/PhysRevLett.61.2484. [Online]. Available: https://link.aps.org/doi/10.1103/PhysRevLett.61.2484.

[56] M. P. Gelfand, R. R. Singh, and D. A. Huse, "Perturbation expansions for quantum many-body systems", *Journal of statistical Physics*, vol. 59, no. 5, pp. 1093–1142, 1990.

[57] G. A. Baker Jr and J. L. Gammel, "The padé approximant", *Journal of Mathematical Analysis and Applications*, vol. 2, no. 1, pp. 21–30, 1961.

[58] D. G. Anderson, "Iterative procedures for nonlinear integral equations", *J. ACM*, vol. 12, no. 4, 547–560, Oct. 1965, ISSN: 0004-5411. DOI: 10.1145/321296.321305. [Online]. Available: https://doi.org/10.1145/321296.321305.

[59] S. Baumann, *Fixedpointacceleration.jl*, https://github.com/s-baumann/FixedPointAcceleration.jl, MIT Expat License, accessed: 2025-09-02, 2018.

[60] P. Löwdin, "Studies in Perturbation Theory. IV. Solution of Eigenvalue Problem by Projection Operator Formalism", *Journal of Mathematical Physics*, vol. 3, no. 5, pp. 969–982, 1962. DOI: 10.1063/1.1724312.

[61] R. P. Feynman, "Forces in molecules", *Phys. Rev.*, vol. 56, pp. 340–343, 1939. DOI: 10.1103/PhysRev.56.340.

[62] F. Verstraete, D. Porras, and J. I. Cirac, "Renormalization algorithms for quantum-many body systems in two and higher dimensions", *Physical Review Letters*, vol. 93, no. 22, p. 227 205, 2004. DOI: 10.1103/PhysRevLett.93.227205.

[63] J. Jordan, R. Orús, G. Vidal, F. Verstraete, and J. I. Cirac, "Classical simulation of infinite-size quantum lattice systems in two spatial dimensions", *Physical Review Letters*, vol. 101, no. 25, p. 250 602, 2008. DOI: 10.1103/PhysRevLett.101.250602.

[64] J. A. Koziol, A. Langheld, and K. P. Schmidt, "Melting of devil's staircases in the long-range dicke-ising model", *Phys. Rev. B*, vol. 111, no. 22, p. 224 427, Jun. 2025. DOI: 10.1103/PhysRevB.111.224427. [Online]. Available: https://link.aps.org/doi/10.1103/PhysRevB.111.224427.

[65] S. Gopalakrishnan, B. L. Lev, and P. M. Goldbart, "Frustration and glassiness in spin models with cavity-mediated interactions", *Phys. Rev. Lett.*, vol. 107, p. 277 201, 2011. DOI: 10.1103/PhysRevLett.107.277201.

[66] P. Strack and S. Sachdev, "Dicke quantum spin glass of atoms and photons", *Phys. Rev. Lett.*, vol. 107, p. 277 202, 2011. DOI: 10.1103/PhysRevLett.107.277202.

[67] V. D. Vaidya *et al.*, "Tunable-range, photon-mediated atomic interactions in multimode cavity qed", *Phys. Rev. X*, vol. 8, p. 011 002, 2018. DOI: 10.1103/PhysRevX.8.011002.

[68] A. A. Houck, H. E. Türeci, and J. Koch, "On-chip quantum simulation with superconducting circuits", *Nature Physics*, vol. 8, no. 4, pp. 292–299, 2012. DOI: 10.1038/nphys2251.

[69] A. Y. Kitaev, "Fault-tolerant quantum computation by anyons", *Annals of Physics*, vol. 303, no. 1, pp. 2–30, 2003. DOI: 10.1016/S0003-4916(02)00018-0.

Von Herzen, in Versen

Mein Dank geht an Professor Schmidt,
der stets mit Rat zur Seite tritt.
Auch Anja, Andi, Max - ihr drei,
ihr wart im Chaos stets dabei.

Im LEP war Stimmung heiter,
Kaffeepausen machten's leichter.
Und Thirsty Thursday - immer fein,
da floss der Spaß ins Herz hinein.

Mit Viktor Training, stark im Gym,
und Sauna danach – Entspannung drin.
Das Ganze war, man glaubt es kaum,
ein Ausgleich, fast schon wie ein Traum.

De'Longhi, Quickmill - Kaffeeduft,
ihr trugt mich durch so manche Kluft.
Und wenn die Arbeit länger stand,
gab Weißes Monster Kraft zur Hand.

Am meisten gilt mein Dank euch zwei,
Mama, Papa - stets dabei.
Mit eurer Liebe, warm und klar,
macht ihr alles möglich, Jahr für Jahr.

Eidesstattliche Erklärung

Hiermit versichere ich, dass ich die vorliegende Arbeit selbstständig verfasst und keine anderen als die angegebenen Quellen und Hilfsmittel benutzt habe, dass alle Stellen der Arbeit, die wörtlich oder sinngemäß aus anderen Quellen übernommen wurden, als solche kenntlich gemacht sind und dass die Arbeit in gleicher oder ähnlicher Form noch keiner Prüfungsbehörde vorgelegt wurde.

Ort, Datum	Jonas Leibig